

1 **Data supporting the North Atlantic Climate System: Integrated Studies (ACSIS) programme,**  
2 **including atmospheric composition, oceanographic and sea ice observations (2016-2022) and output**  
3 **from ocean, atmosphere, land and sea-ice models (1950-2050)**

4 Alex T. Archibald<sup>1, 2</sup>, Bablu Sinha<sup>3</sup>, Maria R. Russo<sup>1, 2</sup>, Emily Matthews<sup>4</sup>, Freya A. Squires<sup>5</sup>, N. Luke  
5 Abraham<sup>1, 2</sup>, Stephane J.-B Bauguitte<sup>6</sup>, Thomas. J. Bannan<sup>4</sup>, Thomas G. Bell<sup>7</sup>, David Berry<sup>8</sup>, Lucy J.  
6 Carpenter<sup>9</sup>, Hugh Coe<sup>4, 10</sup>, Andrew Coward<sup>3</sup>, Peter Edwards<sup>9,11</sup>, Daniel Feltham<sup>12</sup>, Dwayne Heard<sup>13</sup>, Jim  
7 Hopkins<sup>9,11</sup>, James Keeble<sup>1, 2</sup>, Elizabeth C. Kent<sup>3</sup>, Brian A. King<sup>3</sup>, Isobel R. Lawrence<sup>14,15</sup>, James Lee<sup>9,15</sup>,  
8 Claire R. Macintosh<sup>16</sup>, Alex Megann<sup>3</sup>, Bengamin I. Moat<sup>3</sup>, Katie Read<sup>9,11</sup>, Chris Reed<sup>6</sup>, Malcolm J.  
9 Roberts<sup>17</sup>, Reinhard Schiemann<sup>18</sup>, David Schroeder<sup>12</sup>, Timothy J. Smyth<sup>7</sup>, Loren Temple<sup>9</sup>, Navaneeth  
10 Thamban<sup>4</sup>, Lisa Whalley<sup>13,19</sup>, Simon Williams<sup>3</sup>, Huihui Wu<sup>4</sup>, Mingxi Yang<sup>7</sup>

11  
12 <sup>1</sup>National Centre for Atmospheric Science, University of Cambridge, Cambridge, United Kingdom  
13 <sup>2</sup>Yusuf Hamied Department of Chemistry, University of Cambridge, Cambridge CB2 1EW, United Kingdom  
14 <sup>3</sup>National oceanography Centre, United Kingdom.  
15 <sup>4</sup>Department of Earth and Environmental Science, Centre for Atmospheric Science, University of Manchester, Manchester  
16 M13 9PL, United Kingdom  
17 <sup>5</sup>British Antarctic Survey, Cambridge CB3 0ET, United Kingdom  
18 <sup>6</sup>Facility for Airborne Atmospheric Measurements Airborne Laboratory, Cranfield University, Cranfield MK43 0AL, United  
19 Kingdom  
20 <sup>7</sup>Plymouth Marine Laboratory, Plymouth PL1 3DH, United Kingdom  
21 <sup>8</sup>WMO, Geneva, Switzerland  
22 <sup>9</sup>Wolfson Atmospheric Chemistry Laboratories, Department of Chemistry, University of York, York YO10 5DD, United  
23 Kingdom  
24 <sup>10</sup>National Centre for Atmospheric Science, University of Manchester, Manchester M13 9PL, United Kingdom  
25 <sup>11</sup>National Centre for Atmospheric Science, University of York, York, United Kingdom  
26 <sup>12</sup>CPOM, University of Reading, Reading, UK  
27 <sup>13</sup>School of Chemistry, University of Leeds, Leeds LS2 9JT , United Kingdom  
28 <sup>14</sup>ESA ESRIN, Via Galileo Galilei, 1, 00044 Frascati RM, Italy.  
29 <sup>15</sup>CPOM, University of Leeds, Leeds, United Kingdom  
30 <sup>16</sup>ESA Climate Office, United Kingdom  
31 <sup>17</sup>Met Office Hadley Centre, Exeter, UK.  
32 <sup>18</sup>National Centre for Atmospheric Science, Department of Meteorology, University of Reading, Reading, UK  
33 <sup>19</sup>National Centre for Atmospheric Science, University of Leeds, Leeds, United Kingdom

34  
35  
36

37 *Correspondence to:* Alex Archibald ([ata27@cam.ac.uk](mailto:ata27@cam.ac.uk)) and Bablu Sinha ([bablu@noc.ac.uk](mailto:bablu@noc.ac.uk))

38 **Abstract.** The North Atlantic Climate System: Integrated Study (ACSIS) was a large multidisciplinary research programme  
39 funded by the United Kingdom's Natural Environment Research Council (NERC). ACSIS ran from 2016-22 and brought  
40 together around 80 scientists from seven leading UK-based environmental research institutes to deliver major advances in  
41 understanding North Atlantic climate variability and extremes. Here we present an overview of the data generated by the  
42 ACSIS programme. The datasets described here cover the North Atlantic Ocean, the atmosphere above it including its  
43 composition, and Arctic Sea Ice.

44

45 Atmospheric composition datasets include measurements from 7 aircraft campaigns (45 flights in total, 0-10km altitude range)  
46 in the north eastern Atlantic (~40°W-5°E, ~15°N-55°N) made at intervals of from 6 months to 2 years between February 2017  
47 and May 2022. The flights measured chemical species (including greenhouse gases, ozone precursors and VOCs) and aerosols  
48 (organic, SO<sub>4</sub>, NH<sub>4</sub>, NO<sub>3</sub>, and nss-Cl) (<https://dx.doi.org/10.5285/6285564c34a246fc9ba5ce053d85e5e7> (FAAM et al.  
49 (2024)). Ground based stations at the Cape Verde Atmospheric Observatory (CVAO), Penlee Point Atmospheric Observatory  
50 (PPAO) and Plymouth Marine Laboratory (PML) recorded ozone, ozone precursors, halocarbons, as well as greenhouse gases  
51 (CO<sub>2</sub>, methane), SO<sub>2</sub> and photolysis rates. (CVAO, <http://catalogue.ceda.ac.uk/uuid/81693aad69409100b1b9a247b9ae75d5>,  
52 National Centre for Atmospheric Science et al. (2014)), O<sub>3</sub> and CH<sub>4</sub> (PPAO,  
53 <https://catalogue.ceda.ac.uk/uuid/8f1ff8ea77534e08b03983685990a9b0> (Plymouth Marine Laboratory and Yang (2024)) and  
54 aerosols (PML, <https://dx.doi.org/10.5285/e74491c96ef24df29a9342a3d57b5939>, Smyth (2024)).

55

56 Complementary model simulations of atmospheric composition were performed with the UK Earth System Model, UKESM1,  
57 for the period 1982 to 2020 using CMIP6 historical forcing up to 2014 and SSP3-7.0 scenario from 2015-2020. Model  
58 temperature and winds were relaxed towards ERA reanalysis. Monthly mean model data for ozone, NO, NO<sub>2</sub>, CO, methane,  
59 stratospheric ozone tracers and 30 regionally emitted tracers are available to download  
60 (<https://data.ceda.ac.uk/badc/acsis/UKESM1-hindcasts>, Abraham (2024)).

61

62 ACSIS also generated new ocean heat content diagnostics <https://doi.org/10/g6wm>, <https://doi.org/10/g8g2>, Moat et al.  
63 (2021a-b) and gridded temperature and salinity based on objectively mapped Argo measurements  
64 <https://doi.org/10.5285/fe8e524d-7f04-41f3-e053-6c86abc04d51> (King (2023)).

65

66 An ensemble of atmosphere-forced global ocean-sea ice simulations using the NEMO-CICE model was performed with  
67 horizontal resolutions of ¼° and 1/12° covering the period 1958-2020 using several different atmosphere reanalysis based  
68 surface forcing datasets, supplemented by additional global simulations and standalone sea ice model simulations with  
69 advanced sea ice physics using the CICE model (<http://catalogue.ceda.ac.uk/uuid/770a885a8bc34d51ad71e87ef346d6a8>,  
70 Megann et al. (2021e)). Output is stored as monthly averages and includes 3D potential temperature, salinity, zonal, meridional

71 and vertical velocity; 2D sea surface height, mixed layer depth, surface heat and freshwater fluxes, ice concentration and  
72 thickness and a wide variety of other variables.

73

74 In addition to the data presented here we provide a very brief overview of several other datasets that were generated during  
75 ACSIS and have been described previously in the literature.

## 76 **1. The North Atlantic Climate System**

77 The North Atlantic Climate System Integrated Study (ACSIS) was a 6-year research programme (2016-2022) commissioned  
78 by The UK Natural Environment Research Council (NERC) as part of the first wave of a new series of Long Term Science  
79 Multi-centre (LTSM) programmes. ACSIS connected research in the physical and chemical components of the atmosphere-  
80 hydrosphere-cryosphere nexus within the North Atlantic region and provided an opportunity for NERC scientists from  
81 different disciplines to come together and deliver new insights into a region undergoing rapid change in: the ocean and  
82 atmosphere temperatures and circulation, in sea ice thickness and extent, and in key atmospheric constituents such as ozone,  
83 methane and aerosols (Sutton et al., 2018). The ACSIS team included members of the National Centre for Atmospheric Science  
84 (NCAS), Plymouth Marine Laboratory (PML), the National Oceanography Centre (NOC), the British Antarctic Survey (BAS),  
85 the National Centre for Earth Observation (NCEO), the Centre for Polar Observation and Modelling (CPOM), and the Met  
86 Office.

87

88 ACSIS was designed to answer key questions about the North Atlantic Climate System:

89 1) How have changes in natural and anthropogenic emissions and atmospheric circulation combined to shape multi-year trends  
90 in North Atlantic atmospheric composition and radiative forcing? 2) How have natural variability and radiative forcing  
91 combined to shape multi-year trends in the North Atlantic physical climate system? 3) To what extent are changes in the North  
92 Atlantic climate system predictable on multi-year timescales?

93

94 In order to answer these questions, ACSIS was arranged into a series of interlinked work packages involving a broad  
95 representation of scientists from the different NERC centres involved in ACSIS. These work packages delivered new scientific  
96 understanding, delivered through several key synthesis papers (Sutton et al., 2018, Robson et al., 2018, 2020, Hirschi et al.,  
97 2020) as well as a wealth of data. The objectives of ACSIS were:

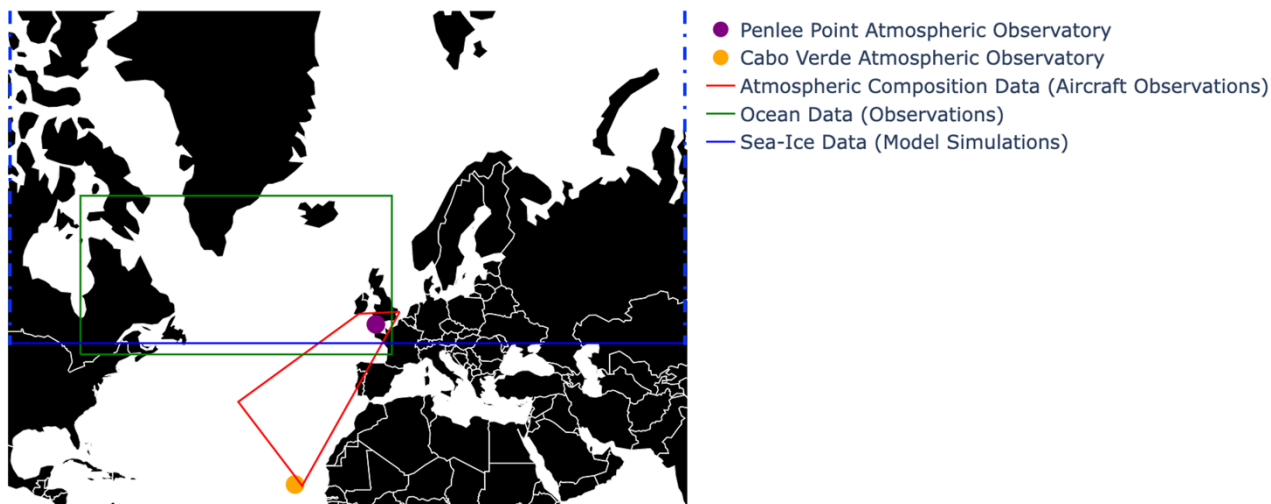
98 A) To provide the UK science community with sustained observations, data syntheses, leading-edge numerical simulations  
99 and analysis tools to facilitate world-class research on changes in the North Atlantic climate system and their impacts. B) To  
100 provide a quantitative and multivariate description of how the North Atlantic climate system is changing. C) To determine the  
101 primary drivers and processes that are shaping changes in the North Atlantic climate system now and will shape changes in  
102 the near future. D) To determine the extent to which future changes in the North Atlantic climate system are predictable.

103 In this paper we focus on objective (A) of the ACSIS project, which included the creation of new datasets to underpin the  
104 ACSIS project and support wider work on the North Atlantic climate system by the UK and international science communities.  
105

106 In this paper we outline the underpinning datasets generated as part of the ACSIS project, how they can be obtained (guided  
107 by the FAIR principles (Wilkinson et al., 2016)), and the motivation for their creation.

## 108 **1.1 Overview of data holdings**

109 A summary of the datasets that are generated by ACSIS and freely available to the community is given in Table 1. Note that  
110 the new data presented in this paper are archived across two platforms: the British Oceanographic Data Centre,  
111 <https://www.bodc.ac.uk> (ocean observations) and the Centre for Environmental Data Analysis, <https://www.ceda.ac.uk> (all  
112 other data). A schematic map giving an overview of the footprints of all the observational datasets can be found in Fig 1. The  
113 three general areas covered are: atmospheric composition covering aircraft and ground station data along with nudged historical  
114 atmospheric chemistry/circulation model simulations; ocean observations covering gridded *in situ* temperature and salinity (0-  
115 2000m) and 0-1000m heat content; forced historical ocean-ice simulations at eddy permitting and eddy resolving resolutions  
116 and standalone Arctic sea ice simulations. In subsequent sections 2, 3 and 4, we describe the individual archived datasets in  
117 detail. Several other datasets, previously described in the literature, have been generated by the ACSIS programme including  
118 simulations to generate volcanic forcing data for climate models, coupled climate model simulations with a high resolution  
119 atmosphere and/or ocean, gridded sea-surface temperature based on *in situ* ocean observations, and observation based estimates  
120 of the Atlantic Meridional Overturning Circulation and Arctic wide sea ice thickness. We anticipate that all the different types  
121 of data used here could be used in synergy and users should take into account the different uncertainties associated with the  
122 different datasets. In particular modelled ice, ocean and atmospheric composition are forced by a variety of different  
123 atmospheric meteorological data, and this may introduce some further uncertainty into attribution of trends and variability  
124 across the different realms. For completeness, and because the new datasets described here will likely be used in conjunction  
125 with the already published datasets, we provide a very brief overview of the latter in Section 5.



126  
127 **Figure 1.** Schematic overview of the footprints of all the observational datasets presented in this paper.  
128

129 **Table 1.** Overview of the data described in this paper with links to the sub-sections where the data are described in detail.

Title	Data, weblink, and citation	Accessibility	Subsection
Aircraft missions	Gas and aerosol data collected on board the Facility for Airborne Atmospheric Measurements <a href="https://catalogue.ceda.ac.uk/uuid/6285564c34a246fc9ba5ce053d85e5e7/">https://catalogue.ceda.ac.uk/uuid/6285564c34a246fc9ba5ce053d85e5e7/</a> FAAM et al. (2024)	Open access for merged 10s data; registration/login to CEDA required for full temporal resolution.	2.1
Ground based observational atmospheric composition time series	Atmospheric composition, including ozone, methane, carbon monoxide, VOCs and aerosol parameters from the Cape Verde Atmospheric Observatory (CVAO) <a href="http://catalogue.ceda.ac.uk/uuid/81693aad69409100b1b9a247b9ae75d5">http://catalogue.ceda.ac.uk/uuid/81693aad69409100b1b9a247b9ae75d5</a> National Centre for Atmospheric Science et al. (2014) Penlee Point Atmospheric Observatory (PPAO) <a href="https://catalogue.ceda.ac.uk/uuid/8f1ff8ea77534e08b03">https://catalogue.ceda.ac.uk/uuid/8f1ff8ea77534e08b03</a>	CVAO data require registration/login to CEDA. PPAO and PML data are open access.	2.2, 2.3

	983685990a9b0 Plymouth Marine Laboratory and Yang (2024). Plymouth Marine Laboratory <a href="https://catalogue.ceda.ac.uk/uuid/e74491c96ef24df29a9342a3d57b5939">https://catalogue.ceda.ac.uk/uuid/e74491c96ef24df29a9342a3d57b5939</a> Smyth (2024)		
Nudged atmosphere model simulations with atmospheric composition	Simulated atmospheric composition from 1981-2020 with atmospheric circulation nudged to ERA5 reanalysis <a href="https://data.ceda.ac.uk/badc/acsis/UKESM1-hindcasts">https://data.ceda.ac.uk/badc/acsis/UKESM1-hindcasts</a> Abraham (2024)	Open access for selected atmospheric composition variables. Requires registration/login on JASMIN and Met Office MASS account for access to comprehensive dataset.	2.4
Ocean circulation and heat content	Objectively interpolated (gridded) ocean temperature and salinity (0-2000m) <a href="https://doi.org/10.5285/fe8e524d-7f04-41f3-e053-6c86abc04d51">https://doi.org/10.5285/fe8e524d-7f04-41f3-e053-6c86abc04d51</a> King (2023)  Upper Ocean (0-1000m) heat content time series <a href="https://doi.org/10/g6wm">https://doi.org/10/g6wm</a> Moat et al. (2021a) <a href="https://doi.org/10/g8g2">https://doi.org/10/g8g2</a> Moat et al. (2021b)	Open access.	3.1,
Ocean-sea ice and standalone sea ice simulations	NEMO-CICE global ocean simulations with default sea ice physics 1°, 1/4° and 1/12° up to 2020 <a href="https://dx.doi.org/10.5285/119a5d4795c94d2e94f610647640edc0">https://dx.doi.org/10.5285/119a5d4795c94d2e94f610647640edc0</a> Megann et al. (2021b) <a href="https://dx.doi.org/10.5285/a0708d25b4fc44c5ab1b06e12fef2f2e">https://dx.doi.org/10.5285/a0708d25b4fc44c5ab1b06e12fef2f2e</a> , Megann et al. (2021c) <a href="https://dx.doi.org/10.5285/4c545155dfd145a1b02a5d0e577ae37d">https://dx.doi.org/10.5285/4c545155dfd145a1b02a5d0e577ae37d</a> , Megann et al. (2021d)	open access	3.2.2, 4.1

<https://dx.doi.org/10.5285/e02c8424657846468c1ff3a5acd0b1ab> Megann et al. (2022a)

<https://dx.doi.org/10.5285/399b0f762a004657a411a9ea7203493a> (Megann et al. (2022b)

NEMO-CICE global ocean simulations with improved sea ice physics 1/4° up to 2020 and standalone Arctic sea ice simulations:

<http://catalogue.ceda.ac.uk/uuid/770a885a8bc34d51ad71e87ef346d6a8> Megann et al. (2021e)

## 130 2. Composition data sets

131 The composition of the atmosphere is changing at an unprecedented pace. Changes in the levels of stratospheric ozone, surface  
132 ozone and other secondary pollutants are driven by human activities (e.g., Griffiths et al., 2021; Keeble et al., 2020; Turnock  
133 et al., 2020). The North Atlantic region has undergone significant growth and decline in air pollution over the last three decades  
134 and modelling studies have all shown the significant human health benefits of these more recent reductions (Turnock et al.  
135 2016; Archibald et al., 2017; Daskalakis et al., 2016). But whilst we have a broad understanding of the distribution of key air  
136 pollutants and short-lived climate forcers, our understanding of the variability of these species and their trends is hampered  
137 across the North Atlantic owing to a paucity of observations. The North Atlantic is frequently impacted by the transport of  
138 transboundary pollution from anthropogenic sources and fires (Boylan et al., 2015; Helmig et al., 2015; Kumar et al., 2013),  
139 as well as from local natural marine and shipping emissions (e.g., Yang et al., 2016a). High altitude research stations in the  
140 Eastern North Atlantic in the Azores (Mt. Pico) and Canary Islands (Izána), coastal observatories on the west coast of Ireland  
141 (Mace Head) and in the Cape Verde Islands have provided long term data sets with which to better understand the sources and  
142 processes controlling reactive trace gases and aerosols across the North Atlantic.

143  
144 In ACSIS a series of work packages were conducted to a) further our understanding of the distribution and variability of key  
145 trace gases and aerosols using aircraft campaigns and long-term measurements, b) understand the processes controlling these  
146 and c) improve model simulations, which can be used to forecast the future evolution of these species. In the following sections  
147 we outline the data that were generated to support these objectives.

### 148 2.1 Aircraft campaigns in the North Atlantic

149 During ACSIS approximately biannual gas and aerosol composition measurements on aircraft missions from the UK to the  
150 Azores were made, focusing on obtaining vertical context for composition, to complement surface observations and provide

151 linkage with satellite data.

152

153 Measurements were collected using the UK's Atmospheric Research Aircraft (ARA). The ARA is a BAe-146-301 which has  
154 been in service since 2004 and is managed by the Facility for Airborne Atmospheric Measurements (FAAM), an airborne  
155 laboratory funded by the UK government. The FAAM aircraft is capable of carrying a 4-tonne instrument load and can operate  
156 at altitudes between 50 and 30000 ft (15–9140 m), allowing the study of processes in the troposphere and boundary layer.  
157 ARA missions as part of ACSIS provide the longest record of composition change in the lower free troposphere over the North  
158 Atlantic (Sutton et al., 2018) and further complemented historic research flights conducted with the ARA in the region (e.g.,  
159 Parrington et al., 2012; Reeves et al., 2002) and more recent flights by other platforms (e.g., ATom (Wofsy et al., 2018),  
160 NAAMES (e.g., Behrenfeld et al., 2019; Sinclair et al., 2020) and ACE-ENA (Zawadowicz et al., 2021).

161

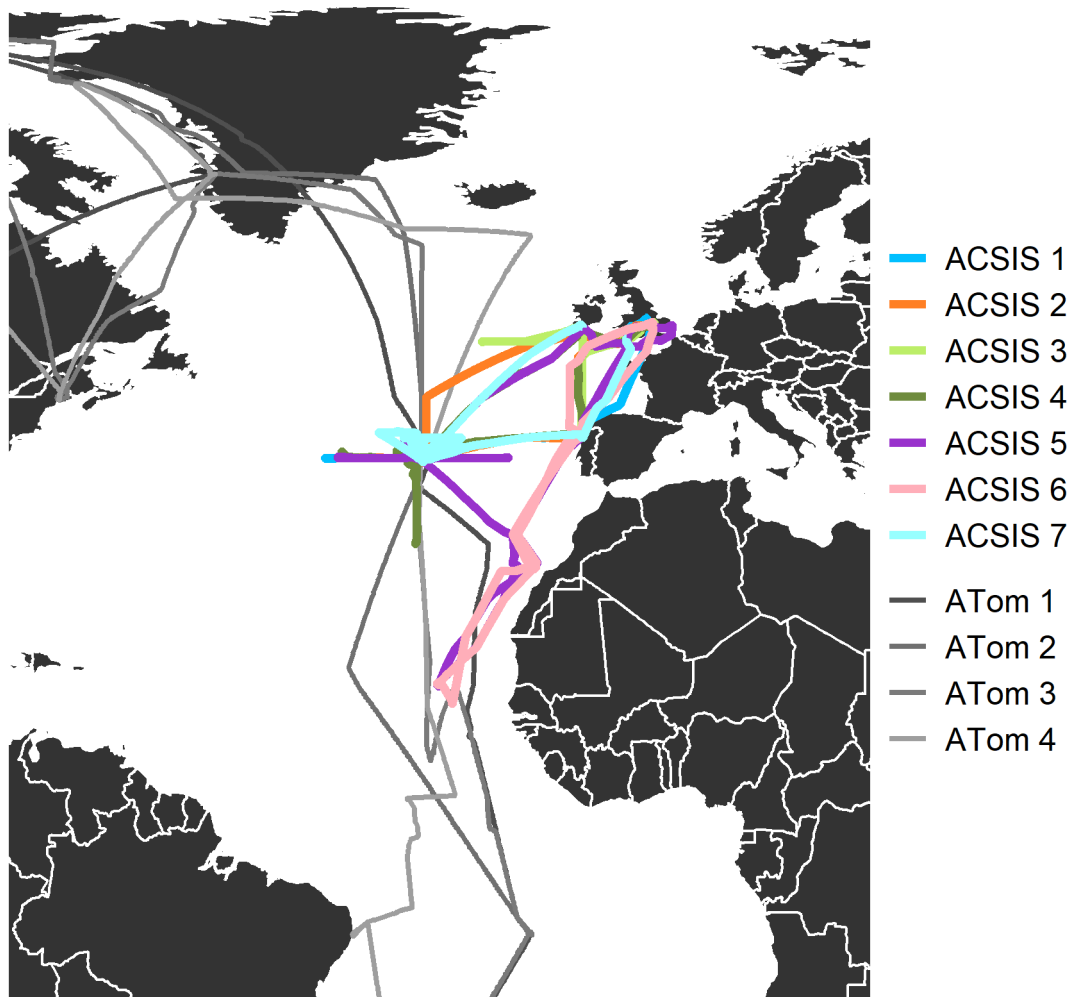
### 162 ***2.1.1 Campaign Flights***

163 A series of (daytime) research flights were carried out across the North Atlantic Ocean from February 2017 – May 2022. Fig.  
164 2 shows the location of the ACSIS flight tracks, coloured by campaign number. There were a total of 45 flights as part of the  
165 ACSIS campaign, comprising close to 200 hours of measurement data. Measurements were made from approximately 50 m  
166 over the sea surface to 9140 m. ACSIS 1, 2, 4, 5 and 7 were predominantly based out of the Azores, whilst flights for ACSIS  
167 3 were based out of Cork, Ireland and ACSIS 6 flights based out of Cape Verde.

168

169 Also shown in Fig. 2 are part of the flight tracks for the NASA Atmospheric Tomography Mission (ATom) mission. The  
170 ATom campaigns aimed to improve the representation of reactive gases and short-lived climate forcers in global atmospheric  
171 chemistry and climate models by measuring atmospheric composition along a global circuit flight track (Prather et al., 2017).  
172 Four ATom campaigns occurred between August 2016 and May 2018. The ATom data set is complementary to that collected  
173 during the ACSIS flight campaigns; ATom flights provided a broad overview on a global scale, whereas ACSIS flights  
174 intensively measured the North Atlantic region. ACSIS-1 overlapped with ATom2 and ACSIS-2 overlapped with ATom3.





176

177 **Figure 2.** A map of flight tracks for the seven ACSIS ARA campaigns. Part of the NASA ATom flight campaign flight tracks  
 178 are shown in grey for comparison.

179

### 180 **2.1.2 Instrumentation**

181 A wide range of instrumentation are fitted on the ARA, including measurements of key meteorological parameters such as  
 182 temperature, humidity, wind speed and direction as well as a range of in situ trace gas measurements including carbon  
 183 monoxide (CO), ozone (O<sub>3</sub>), oxides of nitrogen (NO<sub>x</sub>=NO+NO<sub>2</sub>), and the greenhouse gases carbon dioxide (CO<sub>2</sub>) and methane  
 184 (CH<sub>4</sub>). Table 2 below summarises the measurement techniques, uncertainties and limit of detection (i.e. precision 3σ) onboard  
 185 the ARA that were used during ACSIS flights.

186 **Table 2.** A summary of atmospheric chemistry instrumentation used during the ACSIS flights onboard the FAAM BAe-146-  
 187 301 Atmospheric Research Aircraft.

Measurement	Instrumentation	Time resolution	Precision $3\sigma$	Uncertainty	Timescale	Data available in merged file
O <sub>3</sub>	Thermo 49i ozone photometer	4 sec	6 ppb	3 ppb / 3%	2017-2021	X
O <sub>3</sub>	2B Technologies Model 205 ozone photometer	2 sec	4 nmol mol <sup>-1</sup>	5 ppb / 3% for O <sub>3</sub> > 100 nmol mol <sup>-1</sup>	2022-present	X
CO	AeroLaser AL5002 (VUV RF)	1 sec	6 ppb	2 ppb	2005-2019	X
CO <sub>2</sub>	Los Gatos Research FGGA (OA-ICOS)	1 sec	1.5 ppm	0.5 ppm	2011-present	X
CH <sub>4</sub>	Los Gatos Research FGGA (OA-ICOS)	1 sec	6 ppb	3 ppb	2011-present	X
NO	Chemiluminescence Quality Design Inc	Air 10 sec	10 ppt	24%	2009-2019	X
NO <sub>2</sub>	Chemiluminescence Quality Design Inc	Air 10 sec	13 ppt	41%	2009-2019	X
NO	Chemiluminescence Quality Design Inc (upgraded)	Air 0.1 sec	30 ppt	24%	2019-present	X
NO <sub>2</sub>	Chemiluminescence Quality Design Inc (upgraded)	Air 0.1 sec	60 ppt	41%	2019-present	X
SO <sub>2</sub>	University of York laser-induced fluorescence sulfur dioxide detector (LIF-SO <sub>2</sub> )	1 sec	225 ppt	15 %	2022-present	X
Solar flux	Actinic Ocean Optics QE Pro, up and downward facing UV-vis (280-700 nm) spectrometers	1 sec	TBC	5 %	2019-present	X
HCHO	LIF pulsed 353.370 nm spectrometer, Thermo Scientific Model TFL 3000 Novawave	1 sec	n/a	n/a	2019-present	

VOCs	Whole Air Samples and offline analysis by GC-FID or GC-MS	n/a			2005-present
<i>Other gases</i>	<i>University of Manchester High Resolution-Time of Flight-Chemical Ionisation Mass Spectrometer (ToF-CIMS)</i>	<i>0.25 sec</i>		<i>10-20%</i>	<i>2019-present</i>
HONO	ToF-CIMS	0.25 sec	n/a	20%	
HCN	ToF-CIMS	0.25 sec		30%	X
BrO	ToF-CIMS	0.25 sec	n/a	40%	
BrCl	ToF-CIMS	0.25 sec	n/a	40%	
CINO <sub>2</sub>	ToF-CIMS	0.25 sec		30%	X
Cl <sub>2</sub>	ToF-CIMS	0.25 sec	n/a	20%	
ClO	ToF-CIMS	0.25 sec	n/a	40%	
HPMTF <sup>§</sup>	ToF-CIMS	0.25 sec	n/a	n/a	
Urea	ToF-CIMS	0.25 sec	30 ppt	25%	X
<i>Submicron Aerosol Composition</i>	<i>University of Manchester Aerosol Mass Spectrometer (AMS)</i>				<i>2019-present (excl. 2020)</i>
Organic	AMS	8-15 sec	0.03 µg/m <sup>3</sup>	38%	X
SO <sub>4</sub>	AMS	8-15 sec	0.03 µg/m <sup>3</sup>	36%	X
NH <sub>4</sub>	AMS	8-15 sec	0.03 µg/m <sup>3</sup>	34%	X
NO <sub>3</sub>	AMS	8-15 sec	0.03 µg/m <sup>3</sup>	34%	X
nss-Cl	AMS	8-15 sec	0.03 µg/m <sup>3</sup>	n/a	X

188 <sup>§</sup>Hydroperoxy methyl thioformate.

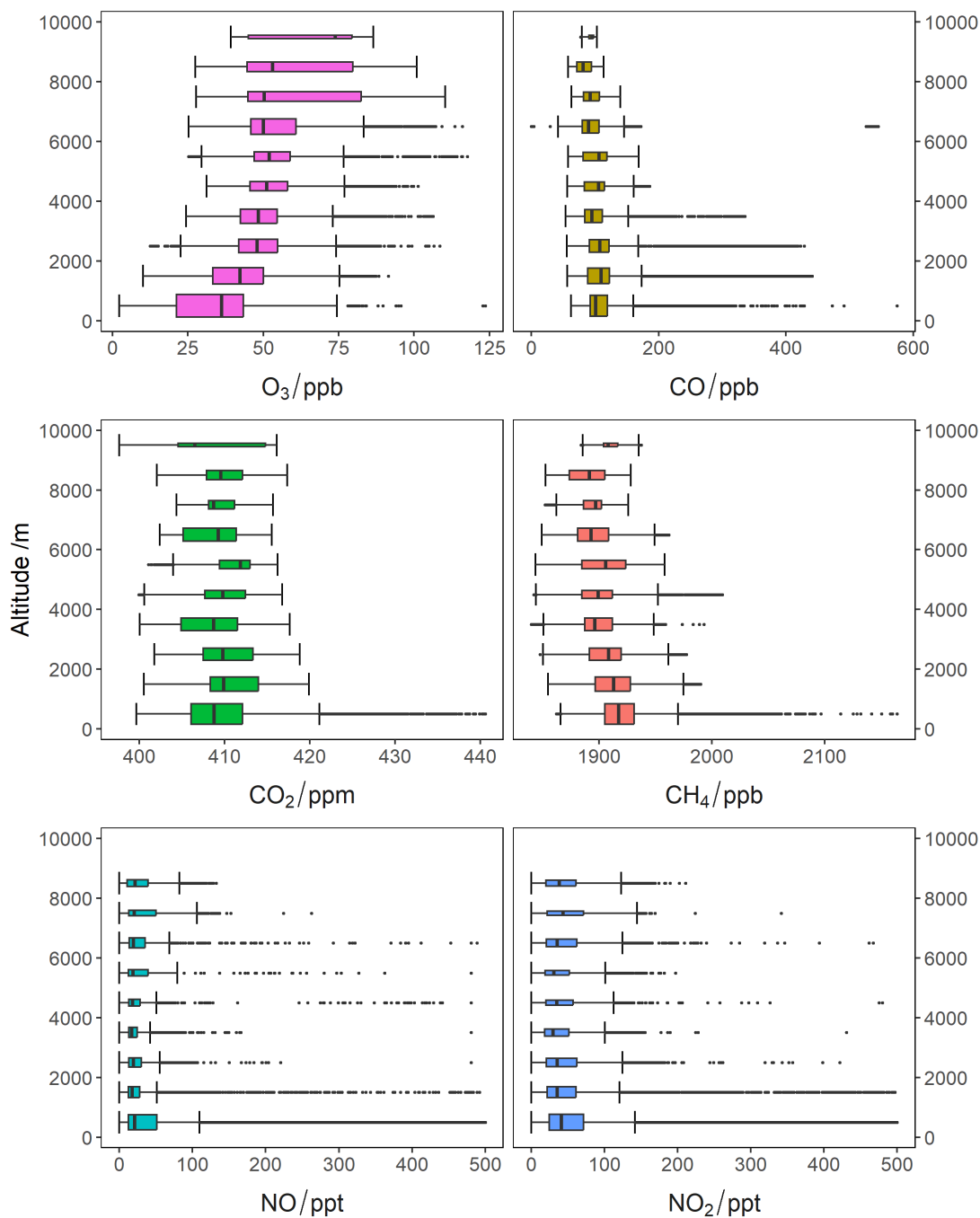
189

### 190 **2.1.3 Vertical Distribution of Pollutants**

191 Data collected during flights from all seven ACSIS campaigns have been analysed together to give insights into the spatial and  
 192 vertical characteristics of atmospheric composition over the North Atlantic Ocean. Data from all seven campaigns have been  
 193 combined and grouped into 1000 m altitude bins. Fig. 3 shows the vertical distribution of O<sub>3</sub>, CO, CO<sub>2</sub>, CH<sub>4</sub>, NO and NO<sub>2</sub>.

194 Table 3 summarises the flights and times that were used in this bulk analysis.

195



196

197 **Figure 3.** Box plots showing the vertical distribution of O<sub>3</sub>, CO, CO<sub>2</sub>, CH<sub>4</sub>, NO and NO<sub>2</sub> for all seven ACSIS campaigns. The  
 198 vertical line in the centre of each box represents the median value with the edges of the boxes showing the 25<sup>th</sup> and 75<sup>th</sup>  
 199 percentiles. The bars extending from the box show the minimum and maximum values no more than 1.5 times the interquartile  
 200 range. The height of the box is proportional to the number of observations within each altitude bin, with taller boxes

201 corresponding to a higher number of observations. Note that sporadic high mixing ratios of CO, NO and NO<sub>2</sub> at low altitudes,  
 202 likely due to local pollution sources, have been filtered so that the bulk of the data is clearly shown. Cut off values of 600  
 203 ppbv for CO and 500 pptv for NO and NO<sub>2</sub> were used. The NO<sub>x</sub> instrument has a ceiling of ~8200 m so there is no data for  
 204 the 9000 – 10000 m bin.

205

206 **Table 3.** Summary of flights used in bulk analysis of atmospheric composition data.

Campaign	Flight Numbers	Date Range	Comments
ACSIS 1	B996, B997, B998, B999, C001, C002	13/02/2017 – 16/02/2017	
ACSIS 2	C066, C067, C068, C070, C071	19/10/2017 – 23/10/2017	
ACSIS 3	C103, C105, C106	14/05/2018 – 17/05/2018	No greenhouse gas data available due to the FGGA fault.
ACSIS 4	C139, C140, C141, C142, C143, C144, C145	19/02/2019 – 22/02/2019	No VOC data on CEDA
ACSIS 5	C199, C200, C201, C202, C203, C204, C205, C210, C211, C212	13/08/2019 – 22/08/2019	
ACSIS 6	C215, C216, C217, C226, C227, C228, C229	04/02/2020 – 14/02/2020	
ACSIS 7	C288, C289, C290, C291, C292, C293, C294	03/05/2022 – 09/05/2022	

207

#### 208 **2.1.4 Data archive**

209 To accompany this paper a 10 second averaged merged file has been created for each flight listed in Table 3  
 210 (<https://catalogue.ceda.ac.uk/uuid/6285564c34a246fc9ba5ce053d85e5e7/>, Facility for Airborne Atmospheric Measurements  
 211 et al., 2024). The merged files are open access and designed to be a tool for an initial exploration of the data and to highlight  
 212 the breadth of the atmospheric composition data collected during the ACSIS programme. However, for further analysis the  
 213 original frequency data should be used and details of where these files can be found is included in the header information of  
 214 the merged files. The merged files are in ascii format and consist of a short explanatory paragraph followed by a list of variables  
 215 and finally the data arranged as columns, with one variable per column with rows corresponding to the values at each 10s time  
 216 interval.

217

## 218 2.2 Cape Verde Atmospheric Observatory (CVAO)

219 ACSIS supported composition measurements at Cape Verde from 2016 to 2021 in order to deliver: quantitative analyses of  
220 composition variability and its relationship to other climate parameters; trend analyses on the long-term surface-based data  
221 sets; understanding of how these link to patterns identified in the aircraft and satellite observations.

222 The Global GAW Cape Verde Atmospheric Observatory is situated in Calhau on the island of Sao Vicente in the Republic of  
223 Cabo Verde (16.848°N, 24.871°W, 10m asl, <https://amof.ac.uk/observatory/cape-verde-atmospheric-observatory-cvao/>).

224 Measurements were started in October 2006 to further our understanding of atmospheric chemistry within the tropical marine  
225 boundary layer and North Atlantic region. The site receives air from a wide variety of sources with 10-day back trajectories  
226 reaching to North America, Europe and sub-Saharan Africa (see Carpenter et al. (2010) for details). Long term high frequency  
227 measurements allow investigation into the trends of climate gases such as CO<sub>2</sub> and CH<sub>4</sub> whilst measurements of pollutants  
228 from the continents such as hydrocarbons and nitrogen oxides provide better constraints of global emission changes and their  
229 effect on the long-term background of the North Atlantic (e.g., Helmig et al., 2016). The Observatory regularly hosts field  
230 campaigns which focus on process studies such as sea-surface interactions and the role of aerosols in atmospheric chemistry  
231 (Read et al., 2008, McFiggans et al., 2009, Lawler et al., 2011, Van Pinxteren et al., 2020).

### 232 2.2.1 Time series of meteorological parameters and chemical composition

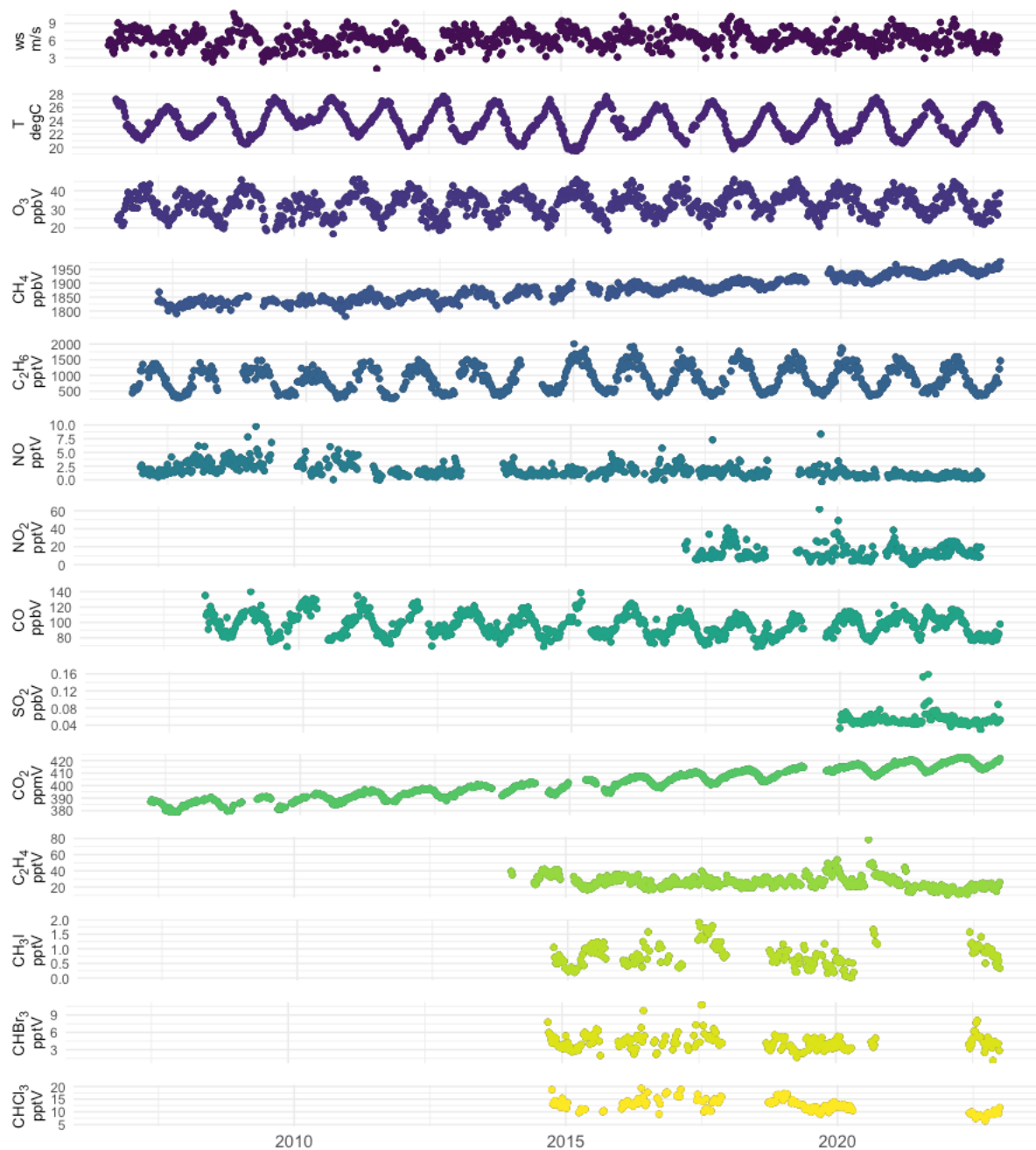
233 Table 4 provides a summary of the chemical species recorded at the CVAO and Fig. 4 shows time series of meteorological  
234 parameters and concentrations of chemical species. During ACSIS these time series were used to estimate trends, particularly  
235 in ozone, carbon monoxide, methane and NO<sub>x</sub>. Here we make some general observations concerning the time series of these  
236 four species. Ozone concentrations at the CVAO show seasonal variability with highest concentrations in spring and lowest in  
237 summer, consistent with its role as a secondary pollutant. In summer, the site occasionally receives air from the southern  
238 hemisphere during the early stages of the Atlantic cyclonic activity, which leads to very low concentrations of ozone (<10 ppb)  
239 observed along with episodes of intense precipitation. Carbon monoxide is a primary pollutant emitted from anthropogenic  
240 sources and from biomass burning. Since 2008 CO has been decreasing at CVAO. Global methane concentrations have  
241 increased substantially over the last 10 years, attributed to increased primary emissions of hydrocarbons and increased  
242 emissions from wetlands due to increasing temperatures (Jackson et al, 2020, Thompson et al., 2018). At CVAO methane has  
243 been increasing steadily. Concerning NO<sub>x</sub>, in extremely clean air containing low levels of CO and VOCs, Andersen et al.  
244 (2022) showed good agreement between NO<sub>2</sub> levels observed at the CVAO and those derived from the photostationary state  
245 (PSS), utilising measured NO, O<sub>3</sub>, and jNO<sub>2</sub> and photo-chemical box model predictions of peroxy radicals. However, in clean  
246 air containing small amounts of aged pollution, as typically encountered in winter, higher levels of NO<sub>2</sub> were observed than  
247 inferred from the PSS, implying underestimation of peroxy radicals or unattributed NO<sub>2</sub> measurement artefacts.

248

249

250 **Table 4.** Summary of atmospheric data recorded at CVAO.

<b>Measurement</b>	<b>Instrumentation</b>	<b>Time resolution</b>	<b>Precision (1hr)</b>	<b>Timescale</b>
O <sub>3</sub>	Thermo 49i ozone monitor	10 sec	0.5 ppb	2006-present
CO	Aerolaser AL5001/ Picarro G4201	4 sec	1 ppb	2008-present
NO	Chemiluminescence instrument Air Quality Design Inc. (AQD), USA	5 min	1.4 ppt	2006-present
NO <sub>2</sub>	Chemiluminescence instrument Air Quality Design Inc. (AQD), USA	5 min	4.4 ppt	2017-present
VOCs	GC-FID	1 hour		2006-present
OVOCs	GC-FID	1 hour		2014-present
Short-lived halocarbons	GC-MS-TOF	1 hour		2014-present
CFCs/HCFCs	GC-MS-TOF	1 hour		2022-present
DMS	GC-FID	1 hour		2012-present
Photolysis rates	Spectral radiometer	1 min		2016-present
CO <sub>2</sub>	Picarro G4201	4 sec	10 ppb	2012-present
CH <sub>4</sub>	Picarro G4201	4 sec	0.3 ppb	2012-present
SO <sub>2</sub>	Thermo 43i HL	5 sec		2019-present
Total Gaseous Mercury	Tekran	1 min		2014-2019



252

253

254

255

256

**Figure 4.** Time series of weekly averaged Cape Verde data showing a range of species and meteorological parameters measured from 7.5m between 2016-2023. From top: wind speed (ws), temperature (T), ozone (O<sub>3</sub>), methane (CH<sub>4</sub>), ethane (C<sub>2</sub>H<sub>6</sub>), nitrogen monoxide (NO), nitrogen dioxide (NO<sub>2</sub>), carbon monoxide (CO), sulphur dioxide (SO<sub>2</sub>), carbon dioxide (CO<sub>2</sub>), ethene (C<sub>2</sub>H<sub>2</sub>), methyl iodide (CH<sub>3</sub>I), bromoform (CHBr<sub>3</sub>) and chloroform (CHCl<sub>3</sub>).



257

### 258 **2.2.2 Data archive**

259 Cape Verde data collected under the auspices of ACSIS is available from CEDA:  
260 <http://catalogue.ceda.ac.uk/uuid/81693aad69409100b1b9a247b9ae75d5> (National Centre for Atmospheric Science et al.  
261 (2014)). Note that there are a number of subdirectories, some of which are not relevant to the data described in this paper. The  
262 relevant subdirectories are labelled with the variable or variable group and the time period (e.g. Cape Verde Atmospheric  
263 Observatory: Ozone measurements (2006 onwards)). The data format is ASCII, consisting of a header explaining the variables  
264 listed followed by the data in columnar format (one column per variable), with the data values in rows appearing in  
265 chronological order. We note that specific Cape Verde data is also archived at the World Data Centre for Greenhouse Gases,  
266 <https://gaw.kishou.go.jp> (CO<sub>2</sub>, CH<sub>4</sub> and CO) and at EBAS, <https://ebas.nilu.no> (VOCs, NO<sub>x</sub>, SO<sub>2</sub> and halocarbons).

### 267 **2.3 Penlee Point Atmospheric Observatory**

268 As with CVAO, ACSIS also supported atmospheric composition observations at Penlee Point, UK. Situated on the eastern  
269 edge of the North Atlantic, the Penlee Point Atmospheric Observatory (PPAO; 50° 19.08' N, 4° 11.35' W;  
270 <https://www.westernchannelobservatory.org.uk/penlee/>) was established by the Plymouth Marine Laboratory (PML) in 2014  
271 on the southwest coast of the United Kingdom. PPAO is a few tens of metres away from the water edge and about 11 m above  
272 mean sea level. The site is exposed to marine air over a very wide sector (wind directions of ~110-260°). Typical southwesterly  
273 winds tend to bring relatively clean background air coming off the North Atlantic, with little terrestrial influence. Winds from  
274 the southeast are often contaminated by exhaust plumes from passing ships, while winds from the north are influenced by  
275 terrestrial emissions. We are particularly interested in the North Atlantic air mass at this coastal location, as this represents the  
276 background condition for the UK during the typical southwesterly conditions.

277 In close proximity to the Western Channel Observatory marine sampling stations, high frequency observations at PPAO enable  
278 both long-term monitoring of trends and process-based studies of atmosphere-ocean interactions. Current/recent work has  
279 assessed trace gas burdens and air-sea fluxes including greenhouse gases (Yang et al. 2016b, 2016c, 2019a), volatile organic  
280 carbon (Phillips et al., 2021), sulfur- (Yang et al., 2016c), halogen- (Sommariva et al., 2018), and nitrogen-containing gases  
281 (ongoing). Further works include aerosol composition and fluxes, with particular foci on ship emissions (ongoing as a part of  
282 the ACRUISE project), sea spray production (Yang et al., 2019b), macro/micro nutrient deposition (White et al., 2021), and  
283 reaction between atmospheric ozone and the sea surface microlayer (Loades et al., 2020).

284 Continuous observations most relevant to ACSIS include ground-based ozone and methane from PPAO as well as column  
285 aerosols from the rooftop of PML (10 km north/northeast of PPAO). These measurements are detailed in Table 5.

286 **Table 5.** Overview of the measurements made at PPAO.

Measurement	Instrumentation	Time resolution	Accuracy	Timescale
O <sub>3</sub>	(a) 2B 205 ozone monitor; (b) Thermo 49i ozone monitor	10 sec	≤1 ppb	(a) May 2014 – Sept 2018 (b) Sept 2018 – present
CH <sub>4</sub>	(a) Picarro G2311-f; (b) Los Gatos Research Fast Greenhouse Gas Analyzer	0.1 sec until Aug 2016; 1 sec since Aug 2016	≤ 3 ppb	(a) May 2014 – Sept 2015 (b) Sept 2015 - present
Aerosols	POM sunphotometer	10 min (when clear sky and during the day)	≤0.01 at 550 nm	2001 – present

287

288

### 289 **2.3.1 Ozone**

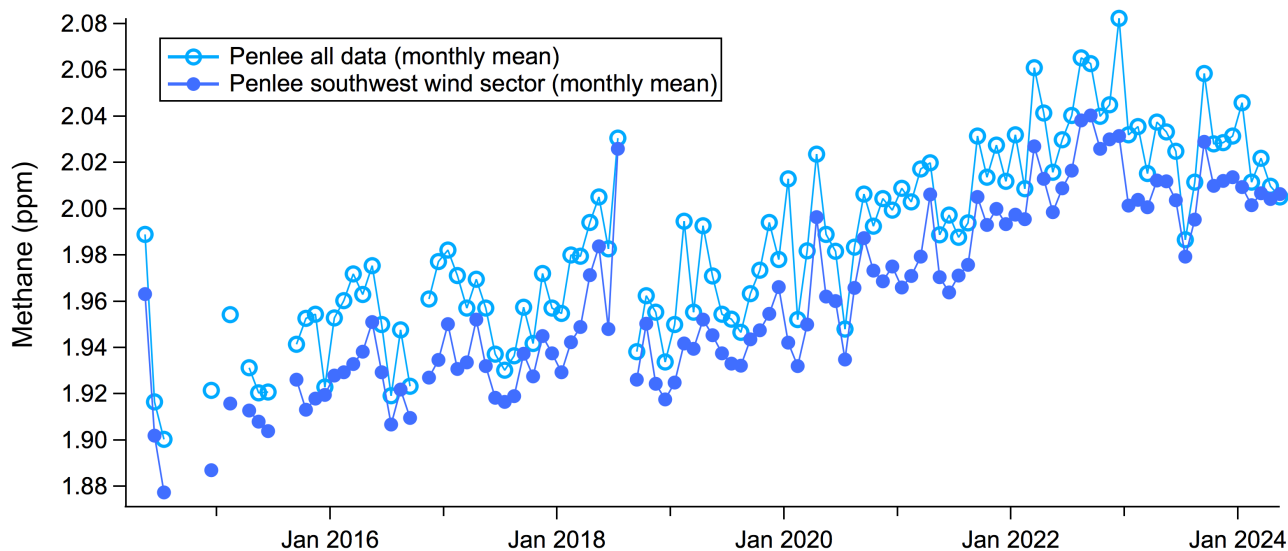
290 Due to the short lifetime of O<sub>3</sub>, it is sensitive to local sources/sinks and heterogeneities associated with a coastal environment.  
 291 This presents a good opportunity to compare two different methods of identifying the southwest (i.e. Atlantic) wind sector: 1)  
 292 by airmass dispersion history (NAME (Numerical Atmospheric-dispersion Modelling Environment) see e.g. Yang and  
 293 Fleming, 2019), and 2) by local wind direction. Data from the first two years of observations (May 2014 to Apr 2016, when  
 294 NAME model output was available) show that defining the PPAO open ocean sector either by local wind direction (210° to  
 295 260°) or by airmass history (>80% in the Atlantic Ocean region over the last 5 days) yield fairly comparable results, with a  
 296 mean difference of about 1.5 ppb. We conclude that the North Atlantic air mass can reasonably be identified from the local  
 297 wind direction between 210° and 260°, and we use this definition in section 2.3.2 below.

298

### 299 **2.3.2 Methane**

300

301 As shown in Figure 5, the overall mean CH<sub>4</sub> mixing ratio is about 0.02-0.03 ppm higher than the mean CH<sub>4</sub> from the southwest  
 302 wind sector (here defined as wind direction between 210° and 260°). This illustrates the importance in considering wind sectors  
 303 in interpretation of coastal observations. The long-term trends in CH<sub>4</sub> mixing ratio are similar with or without the wind sector  
 304 consideration and are in line with observations made globally (e.g., Nisbet et al. 2019). We expect measurements from the  
 305 southwest wind sector to be more representative of the Atlantic and so background Northern Hemisphere. That the all-direction  
 306 mean mixing ratio is higher reflects local and regional emissions of methane.



308

309 **Figure 5:** Long-term measurements of methane from PPAO showing a strong long-term increase.

310

311 Methane shows a mean seasonal amplitude of  $\sim 0.03$  ppm (relative difference of  $\sim 1.5\%$ ). The summer minimum is most likely  
 312 due to an increased sink of methane by the OH radical. These data suggest no significant deviation from the long-term trend  
 313 over the last few years (2019-2022), when it has been postulated that the COVID lockdowns changed the atmospheric oxidising  
 314 capacity and so the OH sink (e.g., Stevenson et al., 2022).

315

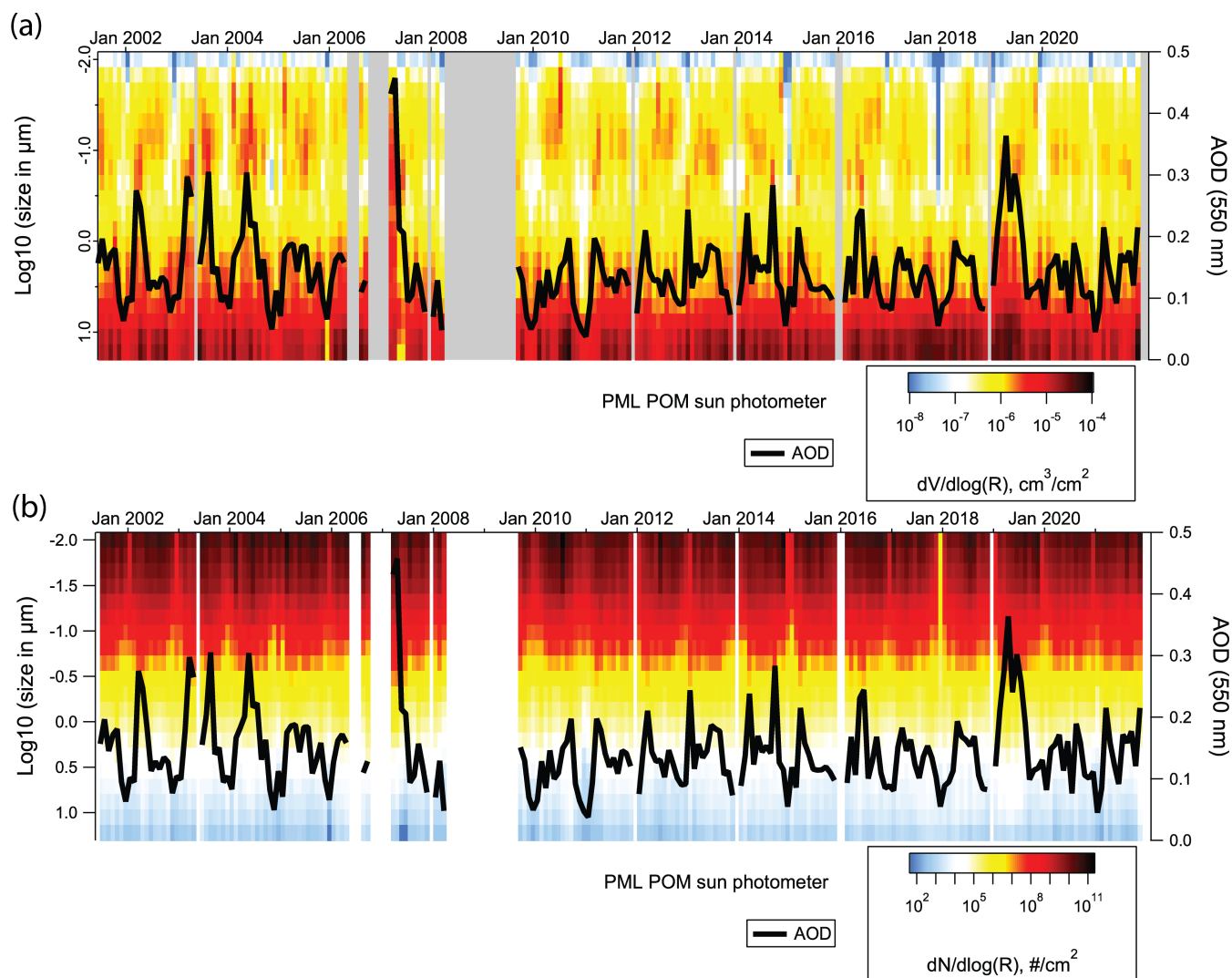
### 316 2.3.3 Aerosols from sunphotometers

317 Long-term aerosol measurements (starting from 2001) have been made from the rooftop of PML ( $50.3661^\circ$  N,  $4.1482^\circ$  W,  
 318 about 10 km NNE of Penlee Point). The retrieved, cloud-filtered data are averaged to monthly intervals as shown in Figure  
 319 6a. Overall there is no obvious long term trend in Aerosol Optical Depth (AOD) at this site, in contrast to many other locations  
 320 in Western Europe that tend to show a gradual reduction. This may be because of the predominance of sea spray aerosols at  
 321 this location (Yang et al. 2020).

322

323 The inferred size distributions are also shown (Fig. 6b). The volume distribution ( $dV/d\log(R)$ ) is dominated by super-micron  
 324 aerosols, while the number distribution ( $dN/d\log(R)$ ) is dominated by sub-micron aerosols. There appears to be a gradual  
 325 reduction in springtime aerosol maximum at around 100 nm radius from 2010 to 2021, which could be related to reduced  
 326 terrestrial or ship anthropogenic emissions (e.g. due to air quality related regulations).

327



328

329 **Figure 6.** Long-term aerosol observations from the PML rooftop (monthly mean). (a) Volume distribution (b) number  
 330 distribution. Thick black line shows the Aerosol Optical Depth (AOD).

331

### 332 2.3.4 Data archive

333 Penlee Point Atmospheric Observatory data is archived at CEDA:  
 334 <https://catalogue.ceda.ac.uk/uuid/8f1ff8ea77534e08b03983685990a9b0> (Plymouth Marine Laboratory and Yang (2024)).  
 335 Data from the PML sun photometer can be found at <https://dx.doi.org/10.5285/e74491e96ef24df29a9342a3d57b5939> (Smyth  
 336 (2024)) The data format is ASCII, consisting of a header explaining the variables listed followed by the data in columnar  
 337 format (one column per variable), with the data values in rows appearing in chronological order.

## 338 2.4 Atmospheric composition modelling with UKESM1

339 To complement the observational data, ACSIS performed climate model experiments with full atmospheric chemistry  
340 included. The experimental design for these simulations was focussed around providing simulations and output that could  
341 support observational campaigns and allowed for a detailed analysis of model transport and composition processes. As well as  
342 all the chemical and aerosol fields, fluxes through all chemical reactions and deposition processes were output as monthly  
343 means. Model restart files were also saved to allow for re-running short sections with an increased (and higher frequency)  
344 output request to compare against flight campaigns. Updates to the experiments were made throughout the project,  
345 incorporating bugfixes and model improvements. The simulations performed are listed in Table 6.

346  
347 Model integrations were performed using a nudged (Telford et al., 2008) configuration of the UKESM1 Earth system model  
348 (Sellar et al., 2019) at Unified Model version 11.5. For nudged model integrations, the horizontal wind fields and potential  
349 temperature are relaxed to either the ERA-Interim (Dee et al., 2011) or ERA-5 (Hersbach et al., 2020) datasets using an e-  
350 folding relaxation timescale of 6 h. Sea-surface temperatures and sea-ice fields were prescribed from the Reynolds dataset  
351 (Reynolds et al., 2002). UKESM simulations were performed using the StratTrop chemical scheme which simulates  
352 the  $O_x$ ,  $HO_x$  and  $NO_x$  chemical cycles and the oxidation of carbon monoxide, ethane, propane, and isoprene in addition to  
353 chlorine and bromine chemistry, including heterogeneous processes on polar stratospheric clouds (PSCs) and liquid sulfate  
354 aerosols (SAs). The two-moment GLOMAP-mode aerosol scheme from UKCA (Mulcahy et al., 2020), is used to simulate  
355 sulfate and secondary organic aerosol (SOA) formation and is driven by prescribed oxidant fields. For further details on  
356 UKESM chemistry and aerosols scheme the reader is referred to Archibald et al. (2020). Simulations were performed from  
357 1981 to 2014 using CMIP historical forcings (labelled as HIST) and continued until 2019 (ERA-Interim) or 2020 (ERA-5)  
358 using SSP3-7.0 forcings (labelled as SCEN) as per the AerChemMIP experiment definition (Collins et al., 2017) (see Table 6)  
359 for details.

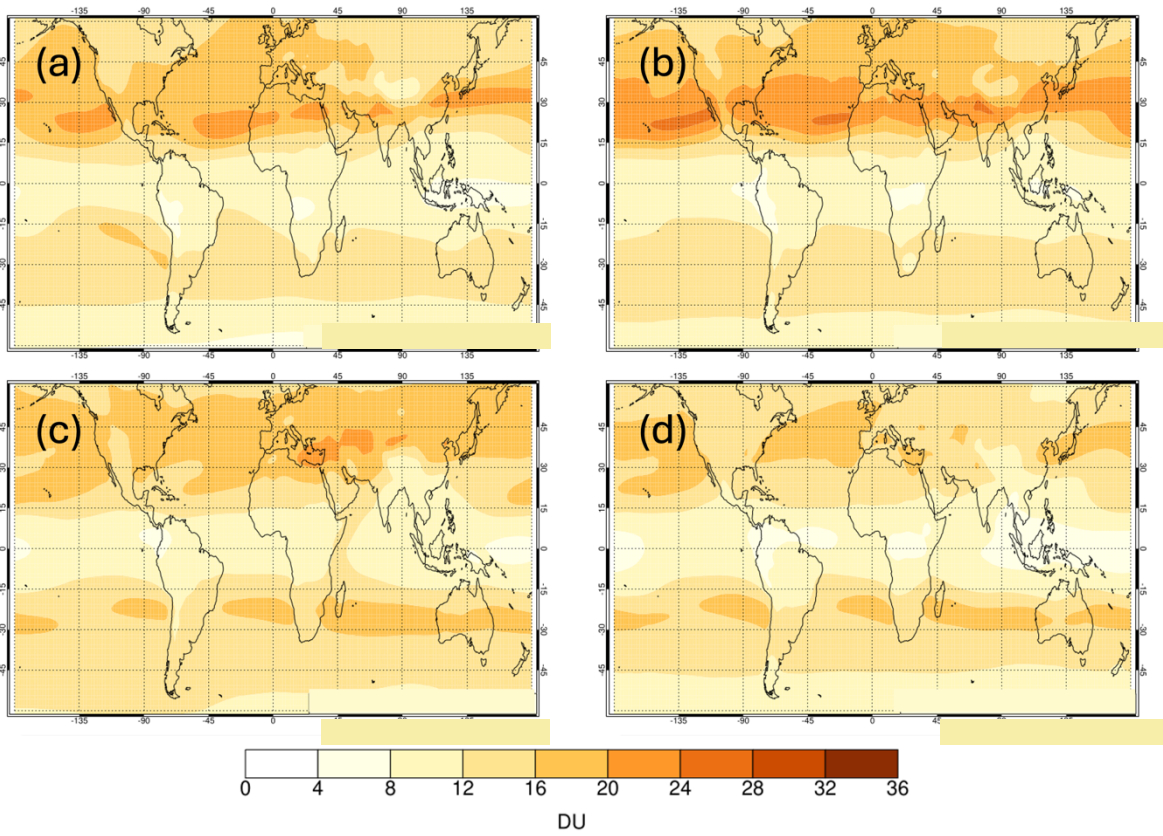
360  
361 In order to identify the impact of transport on modelled tropospheric ozone in the North Atlantic, the following diagnostic  
362 tracers were also defined:

- 363 • 4 different stratospheric ozone tracers ( $O_3s$ ) were added. These are constrained in the stratosphere and evolve freely  
364 in the troposphere where they follow equivalent loss processes to the prognostic ozone field simulated by the model.

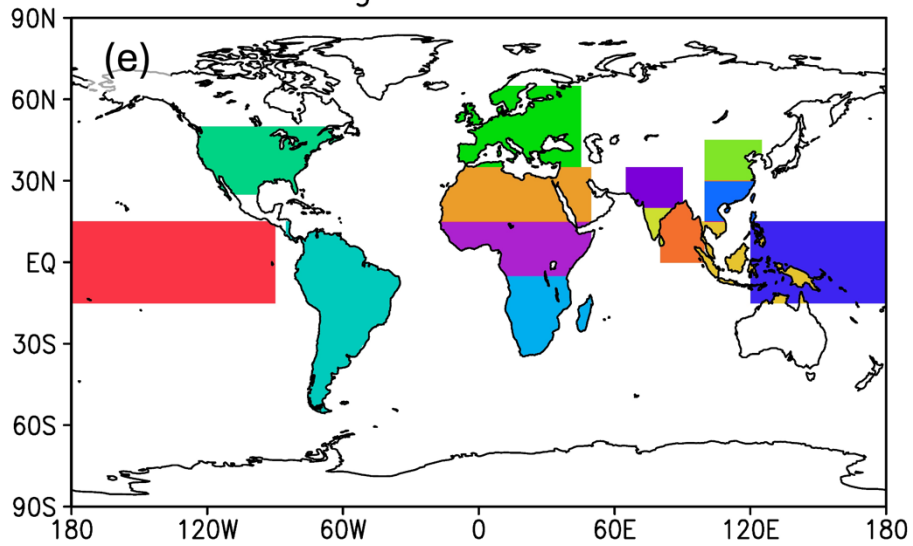
365 The 4  $O_3s$  tracers are described below:

- 366 1. Stratospheric concentrations are set to the prognostic ozone field above a model diagnosed tropopause  
367 defined by the 2PV+380K surface.
- 368 2. Stratospheric concentrations are fixed at 1 ppmv above a model diagnosed tropopause defined by the  
369 2PV+380K surface.

- 370                   3. Stratospheric concentrations are set to the prognostic ozone field above a model diagnosed tropopause  
371                   defined by the WMO tropopause definition.
- 372                   4. Stratospheric concentrations are fixed at 1 ppmv above a model diagnosed tropopause defined by the WMO  
373                   tropopause definition.
- 374 Tracers 1 and 3 are similar to the O<sub>3</sub>s tracers used in the CCM1 experiments (Abalos et al., 2020) and represent tropospheric  
375 ozone originating from the stratosphere, while tracers 2 and 4 (also referred to as constant O<sub>3</sub>s tracers or O<sub>3</sub>s-c) give a  
376 complementary measure of downward transport from the stratosphere that is not affected by stratospheric ozone geographical  
377 distribution or trends (Russo et al., 2023). An example of tracer 1 tropospheric column and its seasonal variation is given in  
378 Figs. 7a-d.
- 379                   • 30 regionally emitted tracers were included to diagnose long range transport into the North Atlantic region. These  
380                   have either a lifetime of 5 or 30 days and emission regions are sketched in Fig. 7e.



Emissions regions for idealised tracers



382

383 **Figure 7.** Integrated tropospheric column O<sub>3</sub>s tracer (in Dobson Units, DU) defined using prognostic ozone and the 2PV+380K  
 384 tropopause, averaged over 2005-2017 using HIST1 and SCEN1 simulations (see Table 6 for details) for (a) December-January  
 385 (DJF) (b) March-May (MAM) (c) June-August (JJA) (d) September-November (SON) e) Emission regions for the 5 day and  
 386 30 day regional tracers.

387

388 **Table 6.** Description of the UKESM1 model simulations.

<b>Simulation</b>	<b>Nudging Dataset</b>	<b>Time Period</b>	<b>Notes</b>	<b>Rose suite ID</b>
HIST1	ERA-Interim	1981-2014	Settings as per UKESM1.	u-bv711 (01/1981-11/1991) and u-bw316 (12/1991-12/2014)
HIST2	ERA-5	1982-2014	Includes code-changes described in Ranjithkumar et al. (2021)	u-bw784 (01/1982-12-2014)
HIST3	ERA-5	1982-2014	Includes code-changes described in Ranjithkumar et al. (2021), technical improvements to the top-boundary condition of the tracers, updated photolysis rates, and the improved heterogeneous chemistry of Dennison et al. (2019)	u-bv828 (01/1982-05/2008) and u-bx320 (06/2008-12/2014)
SCEN1	ERA-Interim	2015-2019	Continuation of HIST1	u-by117 (SSP3-7.0)
SCEN2	ERA-5	2015-2020	Continuation of HIST2	u-by803 (SSP3-7.0)
SCEN3	ERA-5	2015-2020	Continuation of HIST3	u-by808 (SSP3-7.0)

389

#### 390 **2.4.1 Data archive**

391 892 Tb of UKESM1 model data were generated through the ACSIS project. A huge number of model diagnostics were output,  
 392 including high time frequency fields (hourly) across the North Atlantic basin. These are listed here:  
 393 <https://www.ukca.ac.uk/wiki/index.php/ACIS/u-bv711/STASH>. Owing to the large nature of the model data set, selected  
 394 core chemical species and tracers are available to download as monthly mean files from the CEDA dataset  
 395 <https://data.ceda.ac.uk/badc/acsis/UKESM1-hindcasts>, Abraham (2024). These include ozone and ozone precursors (O<sub>3</sub>, NO,  
 396 NO<sub>2</sub>, CO and methane) and the idealised tracers used to diagnose transport in the North Atlantic (four stratospheric tracers and



397 thirty regionally emitted tracers). This data is available for all the model runs described in Table 6. The data is in Met Office  
398 PP format, which can be read using open access Python libraries held at <https://ncas-cms.github.io/cf-python>. If desired, users  
399 may also apply for a Met Office MASS (offline tape archive) account on the UK JASMIN data facility (<https://jasmin.ac.uk>)  
400 and search the Rose Suite IDs given in Table 6 for access to data from the specific experiments performed.

### 401 **3 Ocean data sets**

402 The North Atlantic Ocean is a major component of the overall North Atlantic Climate system and one of the key objectives of  
403 the ACSIS programme was to document the significant changes in ocean circulation and heat content which have taken place  
404 since the mid 20<sup>th</sup> century, to investigate the physical processes responsible and to identify their external drivers. Another  
405 objective was to understand how the ocean might change in the next several decades and to evaluate the potential impacts of  
406 these changes on human society and activities. In order to fulfil these objectives, we compiled a substantial number of new  
407 data products and new model simulations.

408  
409 The data products were compiled on the underlying principle of estimating components of the North Atlantic heat budget plus  
410 the sea surface temperature and sea surface height (dynamic and thermosteric) as these latter two are key to the wider impacts  
411 of the ocean on the atmosphere and on coastal sea level. Thus we brought together a new water mass preserving objectively  
412 interpolated ocean temperature and salinity dataset based on the international Argo float array described in Section 3.1 below  
413 (King, 2023) with two basin scale observational estimates of the horizontal ocean volume and heat transports at 26°N and at  
414 ~55°N described in previous publications (RAPID - <https://rapid.ac.uk/rapidmoc/>, McCarthy et al 2015; Moat et al., 2020,  
415 2022 and OSNAP - <https://www.ukosnap.org/>, Lozier et al., 2019) and a new high spatial and temporal resolution Atlantic sea  
416 surface temperature dataset previously described by Williams and Berry (2020). On the modelling side, we undertook new  
417 cutting edge NEMO forced ocean model simulations with a variety of surface forcing datasets at resolutions of ¼° and 1/12°,  
418 described in Section 3.2, complementary to similar coupled ocean-atmosphere integrations performed at both high and low  
419 atmospheric resolution (previously published and described as an additional dataset in Section 5.2).

#### 421 **3.1 Ocean temperature and salinity, and upper ocean heat content**

422 In order to understand and quantify decadal climate variability and trends in the North Atlantic region, the NOC has produced  
423 new ocean temperature and salinity datasets based on the Argo float array using objectively mapped Argo profiles based on  
424 density levels, which preserve ocean water masses (Desbruyères et al., 2017). The dataset covers the period 2004-present and  
425 extends to depths of up to 2000m. Two versions are available with spatial resolutions of 2° and 1° respectively. During ACSIS  
426 the main use of this dataset has been to calculate subtropical and subpolar heat content alongside other available estimates in  
427 order to understand the interannual to decadal variability of the North Atlantic heat budget (Fig. 8).

428

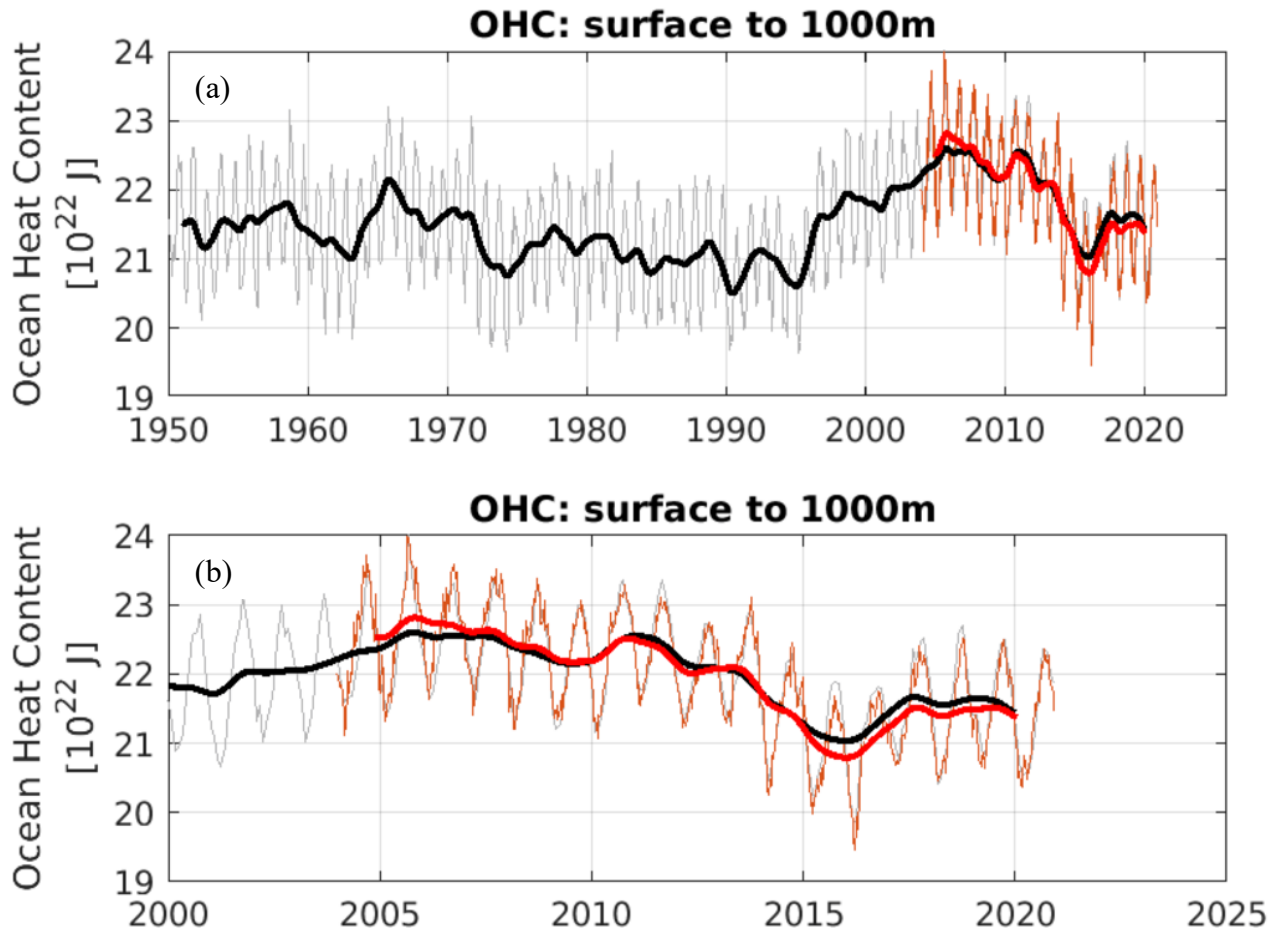


**Figure 8.** Subpolar ocean heat content index in units of  $10^{22}$  J using EN4 (black) and ARGO OI (red) (a) 1950-2020 and (b) during the Argo period 2004-2020). Thick lines have a low pass filter applied with periods variability on periods shorter than 1.8 years removed.

### 3.2 Forced Ocean-ice simulations

Multiple forced ocean-ice simulations were run under ACSIS in order to elucidate the mechanisms of variability seen in the observations (e.g, Fig. 8). A particular emphasis was placed on understanding how uncertainty in surface forcing (meteorological conditions such as windstress and air temperature) impacts predictions of climatically important processes such as the Atlantic Meridional Overturning Circulation (subsection 3.2.1). Another focus was on understanding the impact of modelling at higher (eddy resolving/eddy rich) horizontal resolution on the simulated ocean variability and trends compared to using standard (eddy permitting) resolution (subsection 3.2.2).

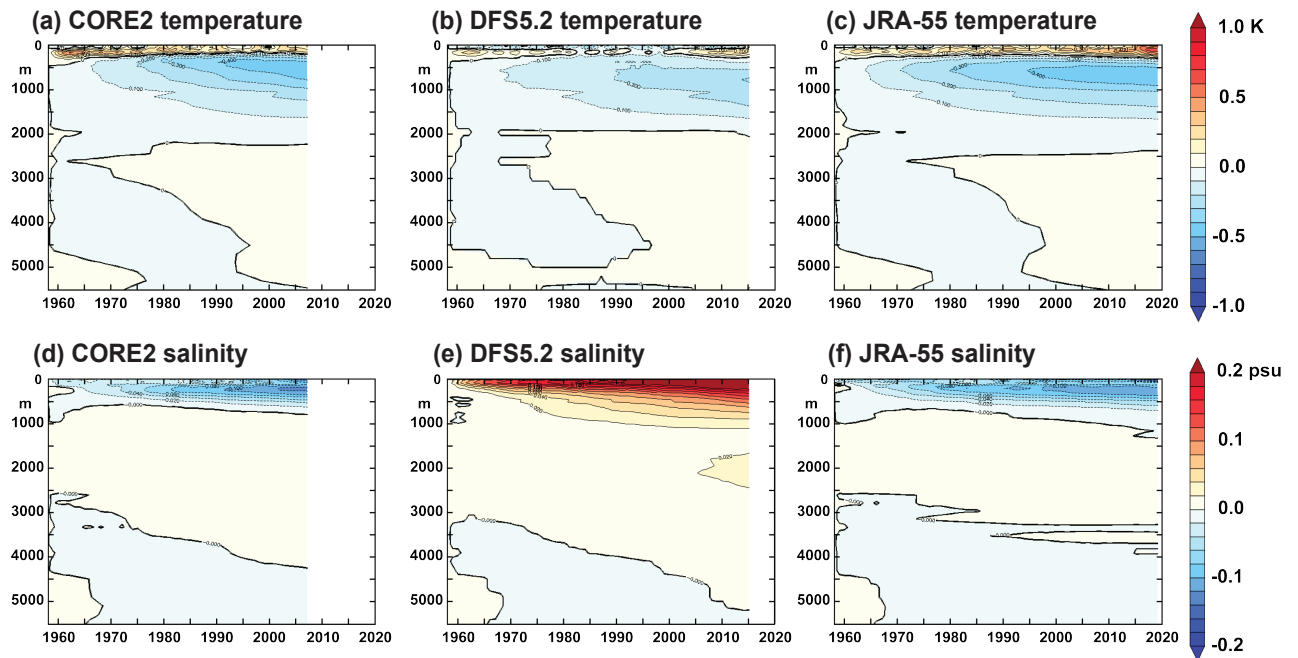
### 463 **3.2.1 1/4° ocean models forced with three different surface meteorological datasets.**

464 Three integrations of a global ocean and sea ice configuration, consisting of Global Ocean v6 (GO6, Storkey et al, 2018) and  
465 Global Sea Ice v8.1 (GSI8.1, Ridley et al, 2018) were carried out to provide a tool for scientific investigation of the mechanisms  
466 of variability of the AMOC and other modes of variability of the Atlantic Ocean. GO6 is based on NEMO v3.6 (Madec 2016),  
467 and GSI8.1 on CICE v5.2.1 (Hunke & Lipscomb, 2010; Ridley et al., 2018) The GO6 ocean configuration was chosen to be  
468 the same as that developed under the JMMP collaborative programme  
469 (<https://www.metoffice.gov.uk/research/approach/collaboration/joint-marine-modelling-programme>) as the ocean component  
470 of the UK's submissions under CMIP6, namely GC3.1 (Williams et al., 2017) and UKESM1 (Sellar et al., 2019), and informed  
471 choices made in the UK OMIP (Ocean Model Intercomparison Project – Griffies et al., 2016) integrations. Three forcing  
472 datasets were used to assess the sensitivity of the models to the choice of forcing data. These were the CORE2 (Large and  
473 Yeager 2009), DFS5.2 (Brodeau et al 2010) and JRA-55 (Tsuji no et al., 2018) datasets, each supplying gridded surface  
474 meteorological variables (air temperature, humidity, and surface winds at subdaily intervals), surface radiative fluxes  
475 (downwelling shortwave and longwave at daily intervals) and freshwater input (snow and precipitation at monthly intervals).  
476 The simulations were run on a global domain on the eORCA025 1/4° grid, with 75 vertical levels. The integrations were run  
477 from 1958 to 2007 (CORE2); from 1958 to 2015 (DFS5.2) and from 1958 to 2020 (JRA-55), and monthly means are archived.  
478 Variables archived include full-depth potential temperature and salinity, horizontal and vertical velocity components, surface  
479 fluxes of heat, freshwater and momentum; mixed-layer depth, sea ice cover and thickness, but many other state and process  
480 variables were also archived. Note that sea ice files from the JRA-forced run are only available for years 1990-2001 and 2002-  
481 2020. These forced ocean-ice simulations use the same configuration as the ocean component of the coupled simulations  
482 described in section 5.2.

483

484 A comparison of the model drifts in globally averaged temperature and salinity is shown in Fig. 9. The reason for showing  
485 model drifts is to alert users to the magnitude and sign of biases present in these model simulations. Biases exist in all model  
486 simulations and must be taken into account when using them to understand historical ocean circulation changes. There is a  
487 large positive drift in upper ocean salinity in the DFS5.2 forced simulation (Fig 9(e)) and a relatively large freshening in the  
488 CORE2 simulation (Figure 9(d)). Overall, the JRA55 forced simulation shows moderate drift in both variables (Figure 9(f)).  
489 This ensemble is thus suitable for understanding the impact of model biases on representation of historical ocean circulation  
490 variability. For example, simulated interannual to multidecadal changes to Atlantic Ocean circulation are similar between the  
491 models despite differences in the mean surface temperature and salinity (Fig 10). More details on the three simulations  
492 including their AMOC variability are given by Megann et al (2021a).

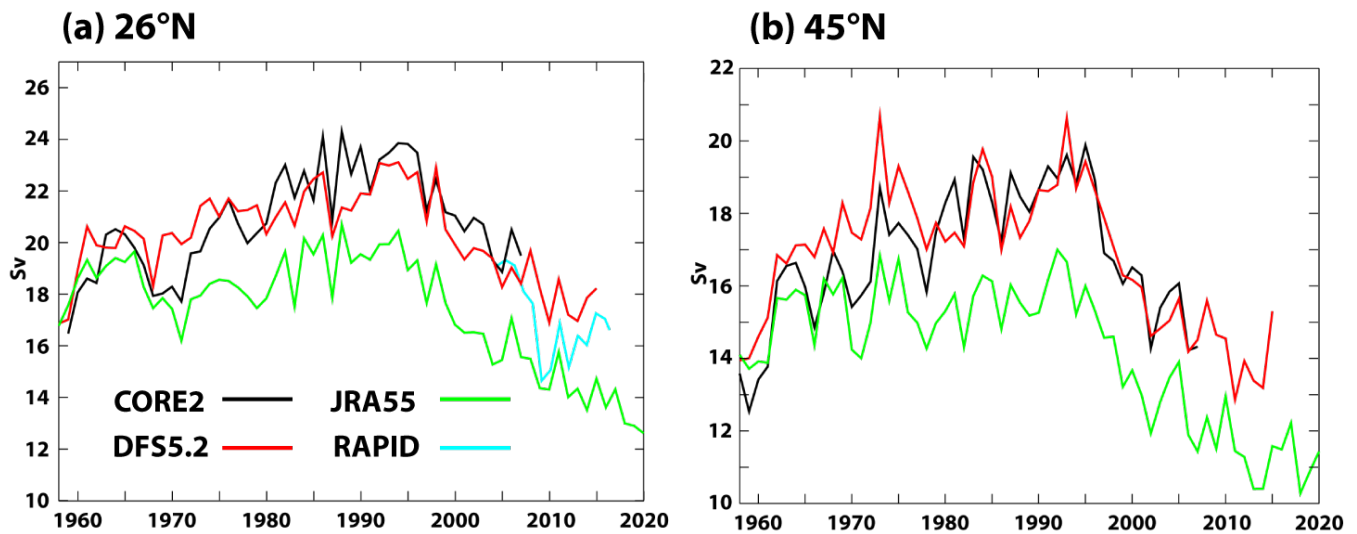
493



494

495 **Figure 9.** Annual drifts in global mean temperature (K), panels (a)-(c) and salinity (psu), panels (d)-(f). (bottom) as a function  
 496 of depth in the ACSIS  $\frac{1}{4}^\circ$  forced ocean model simulations. (a), (d) are from the CORE2 forced simulation, (b), (e) are from  
 497 the DFS5.2 forced simulation and (c), (f) are from the JRA-55 forced simulation.

498



499  
500  
501 **Figure 10.** AMOC timeseries (Sv), 1960-2020 from the ACSIS  $\frac{1}{4}^\circ$  forced ocean model simulations at (a)  $26^\circ\text{N}$  and (b)  $45^\circ\text{N}$ .  
502 Timeseries from all three integrations are shown on each panel: CORE2 forced simulation (black); DFS5.2 forced simulation  
503 (red) and JRA-55 forced simulation (green). The AMOC derived from observations at  $26^\circ\text{N}$  (the RAPID-MOCHA array),  
504 available from 2004 onwards, are plotted in cyan in panel (a).

505  
506 **3.2.2  $\frac{1}{4}^\circ$  and  $1/12^\circ$  “twin” simulations**

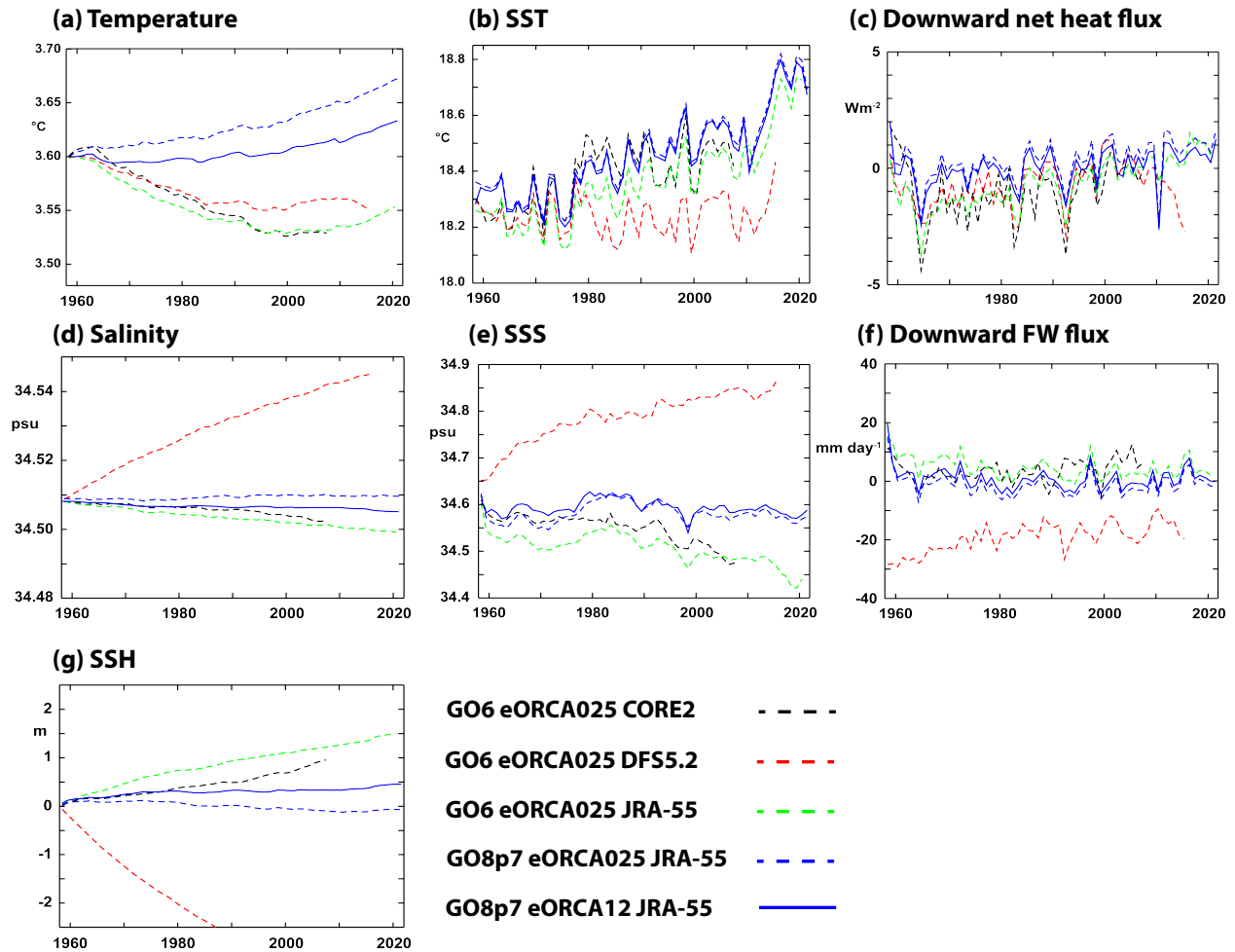
507 Two integrations of the Global Ocean v8p7 (GO8p7) ocean and sea ice configuration simulation were run under the ACSIS  
508 programme. This is based on NEMO v4.0.4 (Madec et al., 2019), including the SI3 sea ice model, and has been developed  
509 under the Joint Marine Modelling Programme (JMMP see  
510 <https://www.metoffice.gov.uk/research/approach/collaboration/joint-marine-modelling-programme>). The simulations are  
511 identical apart from the ocean horizontal resolution: one on a  $\frac{1}{4}^\circ$  grid, and the other a  $1/12^\circ$  grid. They are forced with the  
512 JRA-55 surface forcing dataset (T sujino et al, 2018) from 1958 to 2021. The integrations are intended to provide a tool for  
513 scientific investigation of the mechanisms of variability of the AMOC and ocean heat content of the Atlantic Ocean at an eddy-  
514 rich resolution. The GO8p7 configuration is close to that expected to be incorporated in the GC5.1 coupled climate model and  
515 the UKESM2 earth system model, both aimed at CMIP7. The configuration was implemented at the two resolutions, with the  
516 parameter and physics setting as close as possible (there are some necessary changes to lateral friction which are required for  
517 numerical stability at higher resolution), to investigate the sensitivity of the circulation, numerical mixing and other metrics to  
518 the resolution.

519 As for section 3.2.1 The integrations were carried out on a global domain on eORCA025  $1/4^\circ$  and eORCA12  $1^\circ$  grids, with  
520 75 vertical levels. The integrations were run from 1958 to 2021 and monthly and annual means of the 3-D and 2-D model  
521 fields were saved (including full-depth potential temperature and salinity, horizontal and vertical velocity components, surface

522 fluxes of heat, freshwater and momentum; mixed-layer depth, and sea ice cover and thickness). 5-day means of a selection of  
523 surface fields (including SST, mixed layer depth and sea-surface height) are also archived.

524

525 To illustrate the simulations we show timeseries of some key globally integrated variables from the twin simulations and also,  
526 for context, from the three  $\frac{1}{4}^\circ$  simulations already described in section 3.2.1 (Fig 11). Global mean temperature drifts are of  
527 order 0.05K over the  $\sim 50$  year integrations or  $0.001\text{K yr}^{-1}$ . The  $1/12^\circ$  simulation has a smaller drift than its twin  $\frac{1}{4}^\circ$  resolution.  
528 The twin simulations show positive temperature drift while the other simulations show a negative drift. We expect to see an  
529 SST warming trend under the influence of anthropogenic warming superimposed on interannual and decadal variability. All  
530 the simulations show strong interannual variability with about the same amplitude and timing, forced by interannual changes  
531 in wind stress and buoyancy forcing, and not influenced by global temperature and salinity drifts. On decadal and longer  
532 timescales the difference between variability, secular trends and model drifts can be blurred. The models all show a small  
533 reduction in global mean SST from initialisation to the late 1970s. The DFS5.2 forced simulation then continues to reduce its  
534 SST until the mid 1980s after which the SST remains more or less stable until about 2010, however all the other simulations  
535 increase their SST at a fairly steady rate throughout the 1980s, 1990s and 2000s. From about 2010 onwards all the simulations  
536 experience strong surface warming. Globally integrated downward net surface heat flux (sum of turbulent and radiative  
537 components) is consistent with the global mean surface temperature evolution with a negative net surface flux in the early  
538 decades for the three simulations with different surface flux forcing and a positive net flux for the twin simulations. The net  
539 heat flux for the twin simulations is generally positive whereas for the other simulations it only becomes positive around the  
540 year 2000 and this is when the global mean temperature in those simulations starts to rise. The downward heat flux clearly  
541 shows the signals of large volcanic eruptions (Agung, 1964, el Chichon 1982 and Pinatubo 1991) as well as the 1997 El Nino  
542 event (see Balmaseda et al 2013). The sharp downward dip in 2009 is interesting and possibly linked to the sudden AMOC  
543 reduction at that time, but further research is required to investigate this. With the exception of the DFS5.2 forced simulations,  
544 global mean salinity and global mean surface salinity show quite small trends consistent with a reasonably balanced surface  
545 freshwater flux. The DFS5.2 forced simulation shows strong salinification consistent with a net loss of freshwater through the  
546 surface. The twin runs show best conservation of freshwater. Finally, the net heating/cooling and freshening/salinification of  
547 the simulations is reflected in the global mean sea surface height which is most stable in the twin simulations.



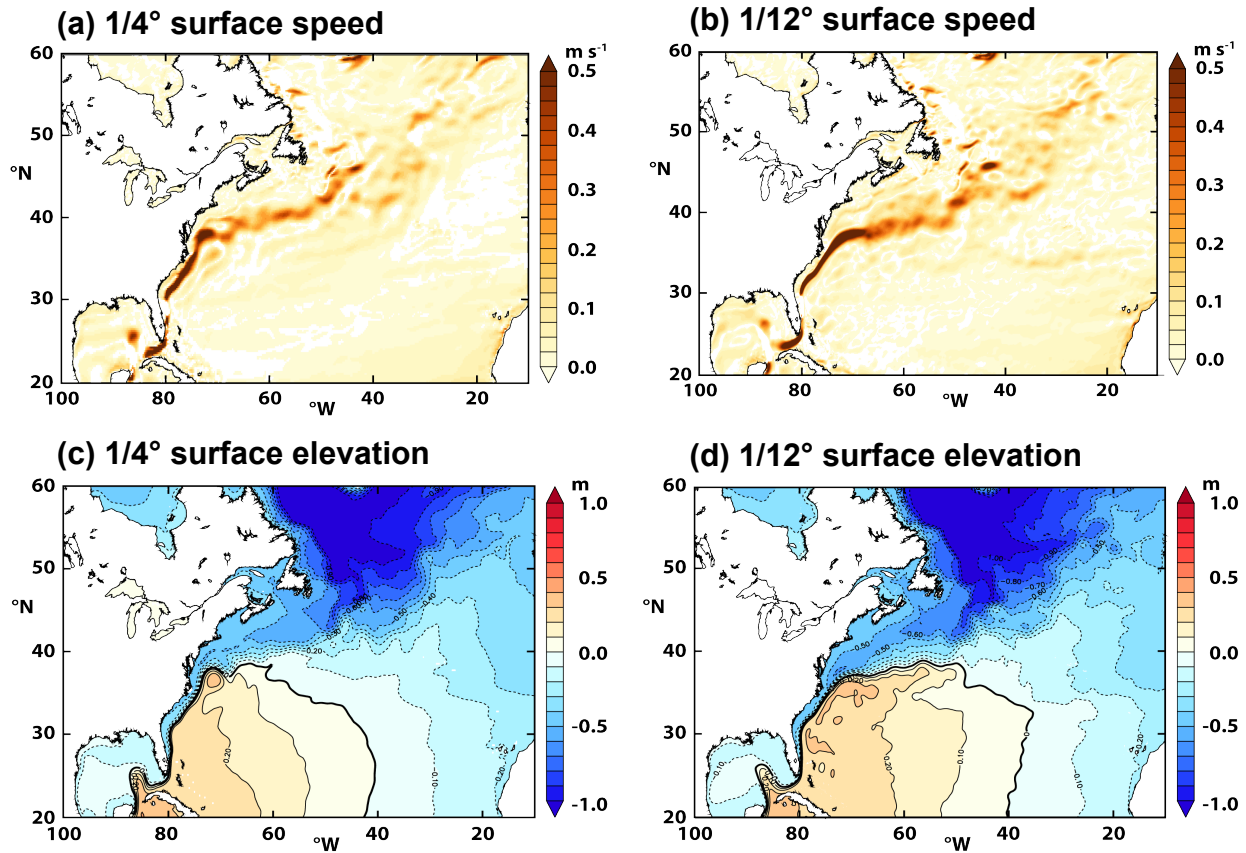
548

549 **Figure 11.** Time series of key variables in the ACSIS  $\frac{1}{4}^\circ$  and  $\frac{1}{12}^\circ$  forced ocean simulations. The variables plotted are:  
 550 (a) global mean temperature; (b) global mean sea-surface temperature; (c) global mean net downward air-sea heat flux;  
 551 (d) global mean salinity; (e) global mean sea-surface salinity; (f) downward freshwater flux; (g) global mean sea-surface  
 552 height. Dashed lines are from the  $\frac{1}{4}^\circ$  model (CORE2 forced – black, DFS5.2 forced – red, JRA-55 forced,  $\frac{1}{4}^\circ$  twin  
 553 simulation – blue) whilst the solid blue line is from the  $\frac{1}{12}^\circ$  twin simulation. Note that the green and blue lines are all  
 554 from JRA-55 forced model simulations but with different model code versions and configurations (see text).

555

556

557



558

559 **Figure 12.** Surface North Atlantic circulation from the ACSIS GO8p7 twin simulations averaged over years 2000-2009.  
 560 Surface speed in  $\text{m s}^{-1}$  for (a) the  $1/4^\circ$  simulation and (b) for the  $1/12^\circ$  simulation; and sea surface height in metres for  
 561 (c) the  $1/4^\circ$  simulation and (d) the  $1/12^\circ$  simulation (bottom right). In panels (c) and (d) the global mean surface height  
 562 has been subtracted to make comparison easier.

563

564 A final illustration shows the mean surface circulation in the North Atlantic from the twin simulations (Fig 12). The most  
 565 obvious difference in the surface current speed (panels (a) and (b)) is that the Gulf Stream separation is more realistic in the  
 566  $1/12^\circ$  simulation where the current moves northeastwards off Cape Hatteras ( $\sim 38^\circ\text{N}$ ). This contrasts with the  $1/4^\circ$  simulation  
 567 where the current shifts direction anticlockwise to remain quite close to the coast. The kink in the Gulf Stream Extension at  
 568 the Northwest corner ( $\sim 50^\circ\text{W}$ ,  $40^\circ\text{N}$ ) is also more realistic in the  $1/12^\circ$  simulation and there is also a discernible signature of  
 569 the Azores current (zonal feature around  $34^\circ\text{N}$ ) which is extremely faint in the  $1/4^\circ$  simulation. Similar features can be seen in  
 570 the mean sea surface height from the two simulations (right panels). One interesting difference is in the penetration of the  
 571 Labrador Current much further south in the  $1/12^\circ$  simulation – where the low sea surface heights characteristic of the subpolar



572 gyre penetrate south west along the North American shelf/slope region north of the Gulf stream extension (between 80°W and  
573 50°W and 35°N to 45°N). Decadal variability in the position of the Gulf Stream has been shown to be linked to salinity  
574 anomalies that are advected southwards by the Labrador Current (New et al., 2022) so these differences between the  
575 simulations are likely to impact on their simulation of AMOC variability.

576

### 577 **3.2.3 Data archive**

578

579 Data from all the ocean simulations are archived in NetCDF format, with four separate files for each month of simulation.  
580 Variables in NEMO are divided into four types which are discretised on slightly different numerical grids. known as the T-  
581 grid for tracers such as temperature and salinity, and the U, V and W grids for the corresponding components (positive  
582 eastwards, northwards and upwards respectively) of the 3D velocity (Madec, 2016, 2019). Each variable has a long name  
583 which gives a detailed description of the variable (see Madec, 2016, 2019 for an explanation of the data output format).  
584 Separate monthly NetCDF files contain sea ice variables on the CICE grid and Lagrangian iceberg properties and trajectories.  
585 The data are archived at CEDA (Megann et al., 2021b, c, d):

586

587 CORE2-forced run: <https://dx.doi.org/10.5285/119a5d4795c94d2e94f610647640edc0> (Megann et al., 2021b),

588 DFS5.2-forced run: <https://dx.doi.org/10.5285/a0708d25b4fc44c5ab1b06e12fef2f2e>,(Megann et al., 2021c)

589 JRA55-forced run: <https://dx.doi.org/10.5285/4c545155dfd145a1b02a5d0e577ae37d> (Megann et al., 2021d)

590 ¼° “twin” simulation: <https://dx.doi.org/10.5285/e02c8424657846468c1ff3a5acd0b1ab> (Megann et al., 2022a)

591 1/12° “twin” simulation: <https://dx.doi.org/10.5285/399b0f762a004657a411a9ea7203493a> (Megann et al., 2022b).

## 592 **4 Ice data sets.**

### 593 **4.1 Advanced Sea Ice model simulations**

594 Results from 6 forced ocean-ice simulations and 2 stand-alone ice simulations are included to document the impact of sea ice  
595 physics and atmospheric forcing data on the Arctic sea ice evolution. All of them use the same sea ice model CICE  
596 configuration GSI8.1 (Ridley et al., 2018) and the ocean-ice simulations use the same ocean model NEMO GO6.0 (Storkey et  
597 al., 2018) as the forced ocean ice simulations of section 3.2 and the HadGEM3 climate model of section 5.2. Three different  
598 atmospheric forcing data sets are applied: NCEP Reanalysis-2 (NCEP2) data (Kanamitsu et al., 2002, updated 2020), CORE2  
599 surface data (Large & Yeager, 2009) and the atmospheric forcing data set DFS5.2 (Dussin et al., 2016). Regarding the sea ice  
600 component, we use the default CICE setup as in HadGEM3 (CICE-default) and an advanced setup (CICE-best) in which a  
601 new process is added (snow loss due to drifting snow) and some adjustments have been made to model physics and parameters.  
602 See Schroeder et al. (2019) and Table 7 for details.

603

**Table 7.** Overview of model simulations with default and improved sea ice processes.

Simulation	Atmospheric forcing	Ocean model	CICE setup	Time period
CICE-default	NCEP2	Mixed-layer	CICEv5.1.2 with prognostic melt pond model and EAP rheology	1980-2020
CICE-best	NCEP2	Mixed-layer	As CICE-default, but with several modifications including snow drift scheme, bubbly conductivity scheme, increased sea ice emissivity and reduced melt pond max fraction parameter (see Schroeder et al., 2019)	1980-2020
NEMO-CICE-1deg-default-CORE	CORE II	NEMOv3.6	CICEv5.1.2 with prognostic melt pond model	1960-2009
NEMO-CICE-1deg-best-CORE	CORE II	NEMOv3.6	As CICE-best	1960-2009
NEMO-CICE-1deg-best-DFS	DFS5.2	NEMOv3.6	As CICE-best	1960-2015
NEMO-CICE-1deg-best-NCEP	NCEP2	NEMOv3.6	As CICE-best	2000-2020
NEMO-CICE-1/4deg-default-DFS	DFS5.2	NEMOv3.6	CICEv5.1.2 with prognostic melt pond model	1979-2015
NEMO-CICE-1/4deg-best-DFS	DFS5.2	NEMOv3.6	As CICE-best, but with increased ice and snow conductivity instead of snow drift scheme	1979-2015

605

606

607

608

609

610

611

612

613

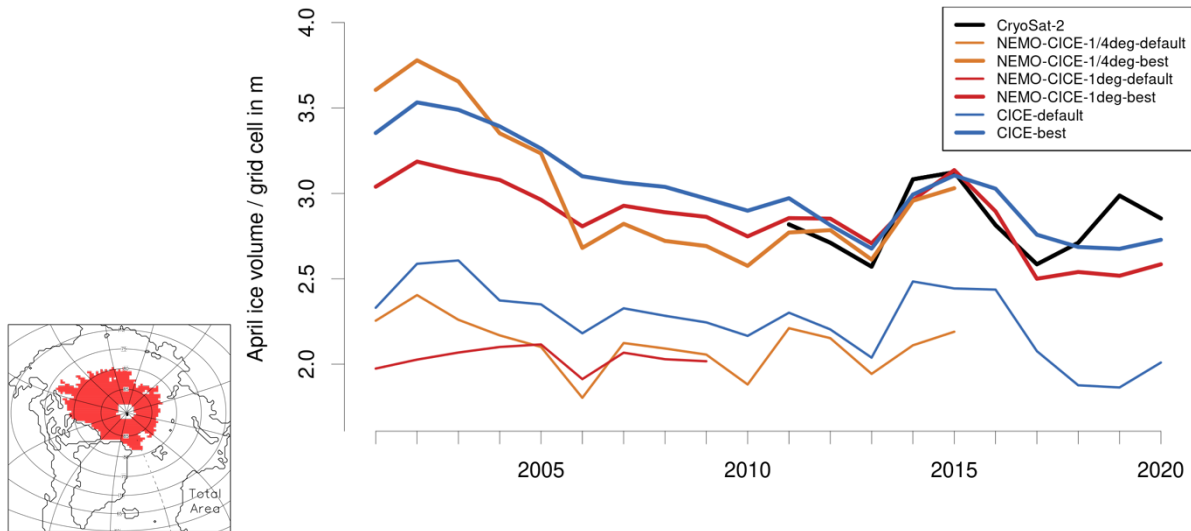
614

615

The impact of our changes to the sea ice model on the fidelity of the model sea ice simulation is shown in Figure 13. All simulations with the default CICE setup (thin lines) underestimate the mean Arctic sea ice thickness during winter. Figure 13 shows that the mean Arctic CryoSat-2 sea ice thickness is more than 50cm thicker in April than in those simulations (see Section 5.3 for the source of our ice thickness estimates). By applying the advanced CICE setup, all simulations (stand-alone, NEMO-CICE 1° and NEMO-CICE 1/4°, thick lines) show realistic mean April sea ice thickness. The advanced setup leads to improvements in simulating summer sea ice extent, too (not shown) and highlights the importance of sea ice physics for accurate model simulations for the Arctic.

#### 4.2 Data archive

616 Data from the global ocean simulations with advanced sea ice are archived in NetCDF format as described in section 3.2.3  
 617 above. Standalone sea ice simulations are similar, but output consists of a single NetCDF file containing sea ice variables on  
 618 the CICE grid for each month of simulation. The data is accessible via CEDA:  
 619 <http://catalogue.ceda.ac.uk/uuid/770a885a8bc34d51ad71e87ef346d6a8> (see Megann et al., 2021e).  
 620



621  
 622 **Figure 13.** Mean April Arctic Sea ice volume per grid cell area over red region for several model simulations in comparison  
 623 to CryoSat-2 estimates. CryoSat-2 thickness are multiplied with sea ice concentration from SSM/I with NASA-Team Bootstrap  
 624 algorithm (Comiso, 2017). The selected region represents the area over which CryoSat-2 data are available for the whole  
 625 period from 2010 to 2020 (October to April). Table 7 provides more information about the setup of the model simulations.  
 626

## 627 5. Synergies with Previously Published Work

628 The new datasets described in the previous sections should be viewed in the context of (and potentially used in conjunction  
 629 with) several other datasets generated in whole or in part by the ACSIS programme and already published and described in the  
 630 scientific literature. Here we provide a very brief overview of these other datasets and include links to where they can be  
 631 accessed. The subsections below correspond to the preceding sections on atmospheric composition (subsection 5.1  
 632 corresponding to Section 2), ocean observations and model simulations (subsection 5.2 corresponding to Section 3), and sea  
 633 ice model simulations (subsection 5.3 corresponding to Section 4).

### 634 5.1 Stratospheric Aerosol Surface Area Density from Explosive Volcanic Eruptions

635 The “MajorVolc” datasets are model simulations within the high-top N96L85 GA4 UM-UKCA composition-climate model  
 636 (Walters et al., 2014) of the monthly progression of the volcanic aerosol clouds from the 3 largest volcanic eruptions of the  
 637 20th century – 1963 Agung, 1982 El Chichon and 1991 Pinatubo. The latter two eruptions fell within the period covered by

638 the UKESM simulations described in Section 2.4, so could be useful in interpreting the aerosol distributions in those  
639 simulations. The simulations are based on the Historical Eruption SO<sub>2</sub> Emission Assessment (HErSEA) experiment protocol  
640 (Timmreck et al., 2018). They apply the v8.2 of the GLOMAP-mode aerosol microphysics module (Mann et al., 2010; Dhomse  
641 et al., 2014; Mann et al., 2015, Brooke et al., 2017; Dhomse et al., 2020) and improve on the CMIP6 volcanic aerosol dataset  
642 (Arfeuille et al., 2013; Luo, 2016). The datasets are described by Dhomse (2020). Dataset identifiers are:  
643 <https://doi.org/10.17632/n3g2htz9hk.1> (Dhomse (2020)); <https://doi.org/10.5281/zenodo.4739170> for Pinatubo (Feng et al.,  
644 2021); <https://doi.org/10.5281/zenodo.4744633> for El Chichon (Dhomse et al., 2021a);  
645 <https://doi.org/10.5281/zenodo.4744686> for Agung (Dhomse et al., 2021b)).  
646

## 647 **5.2 CMIP6 HighResMIP global climate model simulations**

648 All the model and observations based datasets described in Sections 2-4 may be placed in the context of the 6th Coupled Model  
649 Intercomparison Project (CMIP6) HighResMIP (<https://www.highresmip.org/>) sub project (Haarsma et al. 2016, Roberts et al.  
650 2018). The UK contribution to this subproject was based on the HadGEM3 global climate model (Hewitt et al 2011), with a  
651 resolution of ~50 km in the atmosphere and ~0.25° in the ocean. and was delivered as part of the EU Horizon 2020  
652 PRIMAVERA project (<https://www.primavera-h2020.eu/>). The NEMO ocean component in these simulations is the same  
653 configuration as the forced ocean model simulations described in Section 3.2. The HadGEM3 PRIMAVERA simulations most  
654 relevant to this paper were atmosphere only simulations with horizontal resolutions of N256 (~50km) (Roberts (2017a),  
655 <http://doi.org/10.22033/ESGF/CMIP6.6029> and Roberts (2019a), <http://doi.org/10.22033/ESGF/CMIP6.6013>) and N512  
656 (~25km) (Roberts (2017b), <http://doi.org/10.22033/ESGF/CMIP6.6024> and Roberts (2019b),  
657 <http://doi.org/10.22033/ESGF/CMIP6.6008>) and analogous fully coupled simulations with an ocean resolution of 1/4°  
658 (Roberts (2018a), <http://doi.org/10.22033/ESGF/CMIP6.6040>, Roberts (2019c), <http://doi.org/10.22033/ESGF/CMIP6.5984>,  
659 and Schiemann et al. (2019a, b), <http://doi.org/10.22033/ESGF/CMIP6.6041>, <http://doi.org/10.22033/ESGF/CMIP6.5985>).  
660 The simulations were conducted in pairs consisting of a historical simulation from 1950-2014 and a future simulation from  
661 2015-2050. Two further cutting edge simulations were performed at even higher resolution in both ocean and atmosphere,  
662 1/12°, and ~25km (N512) respectively (Roberts (2018b), <https://doi.org/10.22033/ESGF/CMIP6.5881>, and Roberts and  
663 Coward (2018) <https://doi.org/10.22033/ESGF/CMIP6.1822>). The first was a control 1950s climate running from 1950-2014  
664 and the second was a future simulation (SSP5-8.5) from 2015-2050. Roberts et al., (2020) provide an assessment of the  
665 simulated Atlantic Meridional Overturning Circulation in this and other HighResMIP simulations.  
666

## 667 **5.3 Ice observations**

668 Pan-Arctic sea ice thickness is estimated using satellite data from ESA's CryoSat-2 (CS2) mission. Launched in 2010, CryoSat-  
669 2's main payload is a Ku-band radar altimeter (SIRAL), which measures the elevation of Earth's surface. Sea ice freeboard  
670 (the portion of an ice floe above the waterline) is measured by differencing the elevation of the sea ice floe and that of the  
671 surrounding ocean. Sea ice freeboard is then converted to thickness by assuming that sea ice floats in hydrostatic equilibrium

672 in the ocean, and assuming values for snow depth, and snow, ice and ocean density. CryoSat-2's orbit repeats every ~30 days,  
673 providing Arctic-wide sea ice thickness estimates every month from October-April. The method and dataset are detailed in  
674 full in Tilling et al., (2018), and monthly sea ice thickness, gridded at 5km, are available from the CPOM data portal  
675 <http://www.cpom.ucl.ac.uk/csopr/seaice.php>.

676  
677 For the purposes of the ACSIS project, we binned individual CryoSat-2 sea ice thickness estimates provided by CPOM into  
678 the five default ice thickness categories of the sea ice model CICE on a rectangular 50 km grid: (1) ice thickness  $h < 0.6$  m, (2)  
679  $0.6 \text{ m} < h < 1.4$  m, (3)  $1.4 \text{ m} < h < 2.4$  m, (4)  $2.4 \text{ m} < h < 3.6$  m, and (5)  $h > 3.6$  m (Schroeder et al, 2019). The mean area fraction and  
680 mean thickness are then derived for each thickness category. One of the key motivations of binning the CS2 along-track data  
681 into sub-grid ice thickness classes is to assess the role of the ice thickness distribution (ITD) in model initialisation and to  
682 quantify the realism of the CS2 ITD against independent estimates from airborne data. In addition to the bespoke data described  
683 above, monthly (October-April, 2010-2021) 5km-gridded sea ice thickness estimates are available (in ASCII and NetCDF  
684 formats) on the CPOM data portal: <http://www.cpom.ucl.ac.uk/csopr/seaice.php>.

685

## 686 **6 Summary**

687 We have described the multidisciplinary model and observational datasets that were produced by the UK ACSIS programme  
688 and how and where the data can be accessed. The scope of ACSIS was very broad, covering atmospheric composition,  
689 atmospheric circulation, ocean circulation, ice sheets (not covered in this paper), sea ice, and their interactions, and this breadth  
690 is reflected in the rich variety of datasets generated. We note that whilst the focus of the ACSIS programme was the North  
691 Atlantic, most of the model products covered the global domain, and many of the observational products have both global and  
692 regional significance. Despite its great size and scope, the ACSIS programme had finite resources and so was not able to fully  
693 exploit the data it generated. The landmark ACSIS papers cited here can be seen as starting points for further research.  
694 Therefore, we believe there is a major opportunity to repurpose our data for new research studies to build on the substantial  
695 financial and intellectual investment that ACSIS represents, and we express the hope that the ACSIS datasets provide a lasting  
696 legacy to the international environmental science community.

697

## 698 **Appendix A: Overview of select aircraft composition instruments**

### 699 *UoM Time of Flight Chemical Ionisation Mass Spectrometer*

700 The University of Manchester High Resolution-Time of Flight-Chemical Ionisation Mass Spectrometer (ToF-CIMS) is  
701 described in detail by Matthews et al., (2013) for aircraft deployment. Briefly, iodide ions cluster with sample gases in the ion-  
702 molecule reaction region (IMR) region creating a stable adduct. The flow is then sampled through a critical orifice into the  
703 first of the four differentially pumped chambers in the TOF-CIMS, the short segmented quadrupole (SSQ). Quadrupole ion  
704 guides transmit the ions through these stages. The ions are then subsequently pulsed into the drift region of the ToF-CIMS  
705 where the arrival time is detected with a pair of microchannel plate detectors with an average mass resolution of 4000 ( $m/\Delta m$ ).

706 The inlet design is an atmospheric pressure, rearward facing, short residence time inlet, consisting of 3/8" diameter  
707 polytetrafluoroethylene (PTFE) tubing with a total length to the instrument of 48 cm. A constant flow of 12 SLM is mass flow  
708 controlled to the ion-molecule reaction region (IMR) using a rotary vane pump (Picolino VTE-3). 1 SLM is then subsampled  
709 into the IMR for measurement.

710

711 An Iris system as described by Lee et al. (2018) was employed to pressurise and mass flow control the sample flow into the  
712 instrument, avoiding sensitivity changes that would be associated with variations in pressure inflight that is not controlled  
713 sufficiently by the constant flow inlet. This works upon the principle of the manipulation of the size of the critical orifice in  
714 response to changes in the IMR pressure. As with the Lee et al., (2018) design, this works by having a stainless steel plate with  
715 a critical orifice and a movable PTFE plate on top of this, also with a critical orifice. These orifices either align fully and allow  
716 maximum flow into the instrument or misalign to reduce flow. This movement is controlled by the 24VDC output of the IMR  
717 Pirani pressure gauge in relation to the set point and was designed collaboratively with Aerodyne Research Inc. The IMR set  
718 point was  $72 \pm 3$  mbar for the aircraft campaigns which is set through a combination of pumping capacity on the region (Agilent  
719 IDP3), mass flow controlled reagent ion flow and sample flow. The reagent ion flow is 1 SLM of ultra-high purity (UHP)  
720 nitrogen mixed with 2 SCCM of a pressurised known concentration gas mix of CH<sub>3</sub>I in nitrogen, passed through the radioactive  
721 source, <sup>210</sup>Po. The total flow through the IMR is measured (MKS MFM) at the exhaust of the Agilent IDP3 pump so that not  
722 only is the IMR pressure monitored but also the sample flow. All mass flow controllers and mass flow meters are measured  
723 and controlled using the standard Aerodyne Inc EyeOn control unit and software.

724 A pressure controller is also employed on the short segmented quadrupole (SSQ) region to make subtle adjustments in this  
725 region independently of any small IMR changes that may occur inflight. This works upon the principle controlling an  
726 electrically actuated solenoid valve in a feedback loop with the SSQ pressure gauge to actively control a leak of air into the  
727 SSQ pumping line. The SSQ is pumped using an Ebara PDV 250 pump and held at  $1.8 \pm 0.01$  mbar.

728

729 Instrument backgrounds are programmatically run for 6 seconds every minute for the entire flight, by overflowing the inlet  
730 with ultra high purity (UHP) nitrogen at the point of entry into the IMR. Here a 1/16th inch PTFE line enters through the  
731 movable PTFE top plate, ensuring that the flow exceeds that of the sample flow. Inlet backgrounds are also run multiple times  
732 during campaigns manually by overflowing as close to the end of the inlet as possible with UHP nitrogen. Data is taken at 4Hz  
733 during a flight, which is routinely averaged to 1 Hz for analysis. Of the 6 points in each background, the first 2 and last point  
734 are unused and the mean of the background is calculated using custom python scripting. Backgrounds are humidity corrected  
735 and using linear interpolation, a time series of the instrument background is determined and then subtracted to give the final  
736 time series (Matthews, 2023).

737

738 ***UoM Aerosol Mass Spectrometer***

739 The chemical composition of non-refractory submicron aerosols (organic (OA), sulphate, nitrate, ammonium and non-sea-salt  
740 chloride) can be measured by a compact time-of-flight Aerosol Mass Spectrometer (C-ToF-AMS, Aerodyne Research Inc,  
741 Billerica, MA, USA) (Drewnick et al., 2005), which provides chemical characterization across a range of ion mass-to-charge  
742 ( $m/z$ ) ratios from 10 to 500. The detailed operation of the AMS, including calibration and correction factors, during aircraft  
743 deployment has been described previously (Morgan et al., 2009). In brief, aerosols enter the instrument via an aerodynamic  
744 lens inlet, focusing the incoming particles into a narrow beam. The aerodynamic lens system of the AMS in this study is  
745 tailored to sample submicron aerosols. Particles exit the aerodynamic lens into the particle-sizing chamber, which is evacuated  
746 to progressively lower pressures as the particle beam passes through and removes the majority of the gaseous material. Non-  
747 refractory components of the particles are then flash vaporised on a resistively heated porous tungsten surface. The resultant  
748 gaseous molecules are ionised by a 70-eV electron beam released from a tungsten filament. These fragment ions are analysed  
749 by a Time-of-Flight mass spectrometer (ToF-MS). The AMS mass spectra were recorded every 8 or 15 s during the ACSIS  
750 campaign (AC SIS-1 and 3-6). The AMS data was processed using the standard SQUIRREL (SeQUential Igor data RetRiEval,  
751 v.1.65C) ToF-AMS software package. The AMS data was also calibrated using monodisperse ammonium nitrate and  
752 ammonium sulfate particles. A time- and composition-dependent collection efficiency (CE) was applied to the data based on  
753 the algorithm by Middlebrook et al. (2012).

#### 754 *UoY LIF-SO<sub>2</sub>*

755 The University of York LIF-SO<sub>2</sub> instrument is a custom-built system for the highly sensitive detection of SO<sub>2</sub> via laser-induced  
756 fluorescence, and is based on the system originally demonstrated by Rollins et al. (2016). The basic operating principle is the  
757 excitation of SO<sub>2</sub> at 216.9 nm, generated from the fifth harmonic of a custom-built tuneable fibre-amplified semiconductor  
758 diode laser system at 1084.5 nm, and the subsequent detection of the resultant fluorescence photons. The laser wavelength is  
759 rapidly (~10 Hz) tuned on and off a strong SO<sub>2</sub> transition, with the difference between these signals being directly proportional  
760 to the SO<sub>2</sub> concentration within the sample cell. The laser wavelength is tracked using a reference cell containing a known SO<sub>2</sub>  
761 concentration.

762 The ACSIS-7 experiment was part of the first field deployment for the York LIF-SO<sub>2</sub>, and was thus in part a learning experience  
763 on the operation of the instrument aboard an aircraft. The sample flow rate was maintained at 2 slpm and the use of a ram inlet  
764 allowed both the sample and reference cells to be operated at 400 mbar for the full altitude range of the campaign to maximise  
765 instrument sensitivity. Multi-point calibrations were carried out across the expected concentration range approximately every  
766 half an hour to ensure the instrument sensitivity was well characterised. To assess the possible quenching effect of excited SO<sub>2</sub>  
767 by water vapour, or increased wall losses when sampling humid air, calibrations in both stable ambient air and dry zero air  
768 were carried out, for which this effect proved negligible. The uncertainty in the LIF-SO<sub>2</sub> measurements was calculated  
769 predominantly from the uncertainty in the instrument sensitivity (typically 6 %). However, due to inconsistencies in the laser

770 power and laser linewidth, the sensitivity was seen to vary during the course of each flight. Therefore, a mean sensitivity has  
771 been applied and this variation has been conservatively added to the sensitivity uncertainty on a flight-by-flight basis to give  
772 an overall uncertainty of  $\sim 15\%$  (using the mean of this variation). The  $3\sigma$  precision of 225 ppt has also been determined  
773 conservatively from stable ambient measurements due to issues with completely overflowing the instrument inlet with zero air  
774 in flight.

#### 775 **Code/Data availability**

776 Code availability is not applicable for this article. All data is deposited in reliable data repositories and access is detailed in  
777 Table 1 of this article. However, the programs and scripts used for plotting the Figures in this article are stored in a Zenodo  
778 repository: [10.5281/zenodo.13972335](https://doi.org/10.5281/zenodo.13972335).

#### 779 **Author contributions**

780 ATA and BS prepared the original draft with input from TJB, LJC, EM, KR, MRR, FAS, KR, LT, LW, HW, MY  
781 BS, EM and MRR edited the original draft, all authors reviewed the manuscript.  
782 SJB, TJB, EM, CR, FAS, LT, NT, LW, HW acquired data.  
783 ATA, LJC, HC, PE, JL, BS, MY, acquired funding

#### 784 **Competing interests**

785 There are no competing interests.

#### 786 **Acknowledgements**

787 We gratefully acknowledge the financial support provided by the UK Natural Environment Research Council for the extensive  
788 data provided by the ACSIS project. Airborne data were obtained using the BAe-146 Atmospheric Research Aircraft flown by  
789 Airtask Ltd and managed by FAAM Airborne Laboratory, jointly operated by UK Research and Innovation and the University  
790 of Leeds. We would like to give special thanks to the Airtask pilots and engineers and all staff at FAAM Airborne Laboratory  
791 for their hard work in helping plan and execute successful flight campaigns during ACSIS. PE and LT were supported by  
792 NERC awards NE/T008555/1 and NE/S007458/1 for the development and operation of the LIF-SO<sub>2</sub>. MY, TB, and the Penlee  
793 Point Atmospheric Observatory measurements were supported by the NERC projects ACSIS (NE/N018044/1) and MOYA  
794 (NE/N015932/1). TS and the Plymouth sunphotometer measurements were supported by the NERC project ACRUISE  
795 (NE/S005390/1) and by the Western Channel Observatory, which is funded by NERC through its National Capability Long-  
796 term Single Centre Science Programme, Climate Linked Atlantic Sector Science (NE/R015953/1). We further thank Frances



797 Hopkins, Jani Pewter, Daniel Phillips, and Simone Louw for instrument maintenance at Penlee Point Atmospheric  
798 Observatory. We thank Luis Neves, Instituto Nacional de Meteorologia e Geofísica, São Vicente (INMG), Mindelo, Cabo  
799 Verde and, Shalini Punjabi, WACL, for technical assistance in the CVAO measurements. Model simulations were performed  
800 at NCAS, NOC and CPOM under ACSIS grants NE/N018001/1 and NE/N018044/1.

## 801 **References**

802 Abalos, M., Orbe, C., Kinnison, D. E., Plummer, D., Oman, L. D., Jöckel, P., Morgenstern, O., Garcia, R. R., Zeng, G., Stone,  
803 K. A., and Dameris, M.: Future trends in stratosphere-to-troposphere transport in CCM1 models, *Atmos. Chem. Phys.*, 20,  
804 6883–6901, <https://doi.org/10.5194/acp-20-6883-2020>, 2020.

805 Abraham, L.: Data provided by UKESM1 Hindcast simulations for the North Atlantic Climate System Integrated Study  
806 (ACSIS). accessed 31 January 2024, <https://data.ceda.ac.uk/badc/acsis/UKESM1-hindcasts>, 2024.

807 Andersen, S. T. and Nelson, B. S. and Read, K. A. and Punjabi, S. and Neves, L. and Rowlinson, M. J. and Hopkins, J. and  
808 Sherwen, T. and Whalley, L. K. and Lee, J. D. and Carpenter, L. J.: Fundamental oxidation processes in the remote marine  
809 atmosphere investigated using the NO-NO<sub>2</sub>-O<sub>3</sub> photostationary state, *Atmospheric Chemistry and Physics*, 22, (24) 15747-  
810 15765, <https://doi.org/10.5194/acp-22-15747-2022>, 2022.

811  
812 Archibald, A.T., Folberth, G., Wade, D.C. and Scott, D.: A world avoided: impacts of changes in anthropogenic emissions on  
813 the burden and effects of air pollutants in Europe and North America, *Faraday Discussions*, 200, pp.475-500, 2017.

814 Archibald, A.T, M O'Connor, F., Luke Abraham, N., Archer-Nicholls, S., P Chipperfield, M., Dalvi, M., A Folberth, G.,  
815 Dennison, F., S Dhomse, S., T Griffiths, P., Hardacre, C., J Hewitt, A., S Hill, R., E Johnson, C., Keeble, J., O Köhler, M.,  
816 Morgenstern, O., P Mulcahy, J., Ordóñez, C., J Pope, R., T Rumbold, S., R Russo, M., H Savage, N., Sellar, A., Stringer, M.,  
817 T Turnock, S., Wild, O. and Zeng, G.: Description and evaluation of the UKCA stratosphere-troposphere chemistry scheme  
818 (StratTrop vn 1.0) implemented in UKESM1, *Geosci. Model Dev.*, <https://doi.org/10.5194/gmd-13-1223-2020>, 2020.

819 Arfeuille, F. et al.: Volcanic forcing for climate modeling: a new microphysics-based data set covering years 1600–present,  
820 *Climate of the Past*, 10, 359–375, <https://doi.org/10.5194/cp-10-359-2014>, 2014.

821 Balmaseda M. A., Trenberth K. E., Källén E.: Distinctive climate signals in reanalysis of global ocean heat content,  
822 *Geophysical Res. Lett.* 40 (9), 1754–1759, <https://doi.org/10.1002/grl.50382>, 2013.

823 Behrenfeld, M. J., Moore, R. H., Hostetler, C. A., Graff, J., Gaube, P., Russell, L. M., Chen, G., Doney, S. C., Giovannoni, S.,  
824 Liu, H., Proctor, C., Bolaños, L. M., Baetge, N., Davie-Martin, C., Westberry, T. K., Bates, T. S., Bell, T. G., Bidle, K. D.,  
825 Boss, E. S., Brooks, S. D., Cairns, B., Carlson, C., Halsey, K., Harvey, E. L., Hu, C., Karp-Boss, L., Kleb, M., Menden-Deuer,  
826 S., Morison, F., Quinn, P. K., Scarino, A. J., Anderson, B., Chowdhary, J., Crosbie, E., Ferrare, R., Hair, J. W., Hu, Y., Janz,  
827 S., Redemann, J., Saltzman, E., Shook, M., Siegel, D. A., Wisthaler, A., Martin, M. Y., and Ziemba, L.: The North Atlantic  
828 Aerosol and Marine Ecosystem Study (NAAMES): Science Motive and Mission Overview, *Front, Mar. Sci.*, 6,  
829 122, <https://doi.org/10.3389/fmars.2019.00122>, 2019.

830 Boylan, P., Helmig, D., Oltmans, S. and Miller, L.A.: Ozone in the Atlantic Ocean marine boundary layer, *Elementa: Science*  
831 *of the Anthropocene*, 3, 000045, <https://doi.org/10.12952/journal.elementa.000045>, 2015.

832 Brodeau, L. Barnier, B., Treguier, A.-M., Penduff, T., Gulev, S.: An ERA40-based atmospheric forcing for global ocean  
833 circulation models. *Ocean Modelling* 31 (2010) 88–104 ISSN 1463-5003, 2010.

834 Brooke, J. S. A. et al.: Meteoric smoke deposition in the polar regions: A comparison of measurements with global atmospheric  
835 models, *J. Geophys. Res.*, 122, pp. 11,112–11,130, 2017.

836 Carpenter, L. J., Fleming, Z. L., Read, K. A., Lee, J. D., Moller, S. J., Hopkins, J. R., Purvis, R. M., Lewis, A. C., Müller, K.,  
837 Heinold, B., Herrmann, H., et al.: Seasonal characteristics of tropical marine boundary layer air measured at the Cape Verde  
838 Atmospheric Observatory, *Journal of Atmospheric Chemistry*, 67(2), pp.87-140. 2010.

839 Collins, W. J., Lamarque, J.-F., Schulz, M., Boucher, O., Eyring, V., Hegglin, M. I., Maycock, A., Myhre, G., Prather, M.,  
840 Shindell, D., and Smith, S. J.: AerChemMIP: quantifying the effects of chemistry and aerosols in CMIP6, *Geosci. Model Dev.*,  
841 10, 585–607, <https://doi.org/10.5194/gmd-10-585-2017>, 2017.

842 Comiso, J. C., 2017: Bootstrap Sea Ice Concentrations from Nimbus-7 SMMR and DMSP SSM/I-SSMIS, Version 3, 1979–  
843 2022, Boulder, Colorado USA, NASA National Snow and Ice Data Center Distributed Active Archive  
844 Center, <https://doi.org/10.5067/7Q8HCCWS4I0R>.

845 Coward, Andrew; Roberts, Malcolm (2018). *NERC HadGEM3-GC31-HH model output prepared for CMIP6 HighResMIP*.  
846 Version 20240131. Earth System Grid Federation. <https://doi.org/10.22033/ESGF/CMIP6.1822>  
847

848 Daskalakis, N., Tsigaridis, K., Myriokefalitakis, S., Fanourgakis, G. S. and Kanakidou, M.: Large gain in air quality compared  
849 to an alternative anthropogenic emissions scenario. *Atmospheric Chemistry and Physics*, 16(15), pp.9771-9784, 2016.

850 Dee, D. P., Uppala, S. M., Simmons, A. J., Berrisford, P., Poli, P., Kobayashi, S., Andrae, U., Balmaseda, M. A., Balsamo, G.,  
851 Bauer, P., Bechtold, P., Beljaars, A. C. M., van de Berg, L., Bidlot, J., Bormann, N., Delsol, C., Dragani, R., Fuentes, M.,  
852 Geer, A. J., Haimberger, L., Healy, S. B., Hersbach, H., Hólm, E. V., Isaksen, I., Kållberg, P., Köhler, M., Matricardi, M.,  
853 McNally, A. P., Monge-Sanz, B. M., Morcrette, J.-J., Park, B.-K., Peubey, C., de Rosnay, P., Tavolato, C., Thépaut, J.-N., and  
854 Vitart, F.: The ERA-Interim reanalysis: configuration and performance of the data assimilation system, *Q. J. Roy. Meteor.*  
855 *Soc.*, 137, 553–597, <https://doi.org/10.1002/qj.828>, 2011 (data available at: [https://www.ecmwf.int/en/forecasts/datasets/  
856 reanalysis-datasets/era-interim](https://www.ecmwf.int/en/forecasts/datasets/reanalysis-datasets/era-interim), last access: 12 January 2023).

857 Dennison, F., Keeble, J., Morgenstern, O., Zeng, G., Abraham, N. L. and Yang, X.: Improvements to stratospheric chemistry  
858 scheme in the um-ukca (v10. 7) model: Solar cycle and heterogeneous reactions, *Geoscientific Model Development*, 12(3),  
859 pp.1227-1239. 2019.

860 Desbruyères, D., McDonagh, E. L., King, B. A. and Thierry, V.: Global and full-depth ocean temperature trends during the  
861 early twenty-first century from Argo and repeat hydrography. *J. Climate*, 30, 1985–1997, 2017, doi:10.1175/JCLI-D-16-  
862 0396.1.

863 Dhomse, S.: UMUKCA\_Volcanic\_Forcing\_Data\_Dhomse2020, Mendeley Data, V1, <https://doi.org/10.17632/n3g2htz9hk.1>,  
864 2020.

865 Dhomse, S. S. et al.: Aerosol microphysics simulations of Pinatubo eruption with UKCA composition-climate model, *Atmos.*  
866 *Chem. Phys.*, 14, pp. 11221–11246, 2014. <https://doi.org/10.5194/acp-14-11221-2014>, 2014.

867 Dhomse, S. S. et al.: Evaluating the simulated radiative forcings, aerosol properties, and stratospheric warmings from the 1963  
868 Mt Agung, 1982 El Chichón, and 1991 Mt Pinatubo volcanic aerosol clouds, *Atmos. Chem. Phys.*, 20, 13627–13654, 2020,  
869 <https://doi.org/10.5194/acp-20-13627-2020>, 2020.

870 Dhomse, S., Feng, W., Rap, A., Carslaw, K., Bellouin, N., and Mann, G.: SMURPHS/ACSIS El Chichon volcanic forcing  
871 dataset (mapped to UM wavebands) -- from HErSEA ensemble of interactive strat-aerosol GA4 UM-UKCA runs (Dhomse et  
872 al., 2020, ACP) (Version v1) [Data set], Zenodo, <https://doi.org/10.5281/zenodo.4744634>, 2021a.

873 Dhomse, S., Feng, W., Rap, A., Carslaw, K., Bellouin, N., and Mann, G.: SMURPHS/ACSIS Agung volcanic forcing dataset  
874 (mapped to UM wavebands) -- from HErSEA ensemble of interactive strat-aerosol GA4 UM-UKCA runs (Dhomse et al.,  
875 2020, ACP) (Version v1) [Data set], Zenodo, <https://doi.org/10.5281/zenodo.4744687>, 2021b.

876 Drewnick, F., Hings, S. S., DeCarlo, P., Jayne, J. T., Gonin, M., Fuhrer, K., Weimer, S., Jimenez, J. L., Demerjian, K. L.,  
877 Borrmann, S., and Worsnop, D. R.: A new time-of-flight aerosol mass spectrometer (TOF-AMS) – Instrument description and  
878 first field deployment, *Aerosol Sci. Tech.*, 39, 637–658, <https://doi.org/10.1080/02786820500182040>, 2005.

879 Dunstone, N. J., Smith, D. M., and Eade, R.: Multi-year predictability of the tropical Atlantic atmosphere driven by the high-  
880 latitude North Atlantic Ocean. *Geophys. Res. Lett.*, **38**, L14701, <https://doi.org/10.1029/2011GL047949>, 2011.

881 Dussin, R., Barnier, B., Brodeau, L., and Molines, J. M.: The making of the DRAKKAR forcing set DFS5. DRAKKAR  
882 (MyOcean report 01-04-16), LGGE, Grenoble, France, 2016.

883 Facility for Airborne Atmospheric Measurements; Natural Environment Research Council; Met Office; Archibald, A.;  
884 Matthews, E.; Squires, F.; Wu, H.; Temple, L.: ACSIS: Merged airborne chemistry data from instruments on board the FAAM  
885 aircraft. NERC EDS Centre for Environmental Data Analysis, <https://doi.org/10.5285/6285564c34a246fc9ba5ce053d85e5e7>,  
886 2024

887

888 Feng, W., Dhomse, S., Rap, A., Carslaw, K., Bellouin, N., and Mann, G.: SMURPHS/ACSIS Pinatubo volcanic forcing dataset  
889 (mapped to UM wavebands) -- from HERSEA ensemble of interactive strat-aerosol GA4 UM-UKCA runs (Dhomse et al.,  
890 2020, ACP) (v1), <https://doi.org/10.5281/zenodo.4739171>, 2021.

891 Good, S. A., Martin, M. J. and Rayner, N. A.: 2013. EN4: quality controlled ocean temperature and salinity profiles and  
892 monthly objective analyses with uncertainty estimates, *Journal of Geophysical Research: Oceans*,  
893 <https://doi.org/10.1002/2013JC009067>, 2013.

894 Griffies, S. M., Danabasoglu, G., Durack, P. J., Adcroft, A. J., Balaji, V., Böning, C. W., Chassignet, E. P., Curchitser, E.,  
895 Deshayes, J., Drange, H., Fox-Kemper, B., Gleckler, P. J., Gregory, J. M., Haak, H., Hallberg, R. W., Heimbach, P., Hewitt,  
896 H. T., Holland, D. M., Ilyina, T., Jungclaus, J. H., Komuro, Y., Krasting, J. P., Large, W. G., Marsland, S. J., Masina, S.,  
897 McDougall, T. J., Nurser, A. J. G., Orr, J. C., Pirani, A., Qiao, F., Stouffer, R. J., Taylor, K. E., Treguier, A. M., Tsujino, H.,  
898 Uotila, P., Valdivieso, M., Wang, Q., Winton, M., and Yeager, S. G.: OMIP contribution to CMIP6: experimental and  
899 diagnostic protocol for the physical component of the Ocean Model Intercomparison Project, *Geosci. Model Dev.*, **9**, 3231-  
900 3296, <https://doi.org/10.5194/gmd-9-3231-2016>, 2016.

901 Griffiths, P. T., Murray, L. T., Zeng, G., Shin, Y. M., Abraham, N. L., Archibald, A. T., Deushi, M., Emmons, L. K., Galbally,  
902 I. E., Hassler, B., Horowitz, L. W., Keeble, J., Liu, J., Moeini, O., Naik, V., O'Connor, F. M., Oshima, N., Tarasick, D., Tilmes,  
903 S., Turnock, S. T., Wild, O., Young, P. J., and Zanis, P.: Tropospheric ozone in CMIP6 simulations, *Atmos. Chem. Phys.*, **21**,  
904 4187–4218, <https://doi.org/10.5194/acp-21-4187-2021>, 2021.

905 Haarsma, R. J., Roberts, M. J., Vidale, P. L., Senior, C. A., Bellucci, A., Bao, Q., et al.: High Resolution Model Intercomparison  
906 Project (HighResMIP v1.0) for CMIP6, *Geoscientific Model Development*, **9**(11), 4185–4208. <https://doi.org/10.5194/gmd-9-4185-2016>, 2016.

908 Helmig, D., Muñoz, M., Hueber, J., Mazzoleni, C., Mazzoleni, L., Owen, R.C., Val-Martin, M., Fialho, P., Plass-Duelmer, C.,  
909 Palmer, P.I. and Lewis, A.C.: Climatology and atmospheric chemistry of the non-methane hydrocarbons ethane and propane  
910 over the North AtlanticNMHC at Pico Mountain, *Elementa: Science of the Anthropocene*, **3**, 54, ISSN 2325-1026, 2015.

911 Helmig, D., Rossabi, S., Hueber, J. et al.: Reversal of global atmospheric ethane and propane trends largely due to US oil and  
912 natural gas production, *Nature Geosci* **9**, 490–495, <https://doi.org/10.1038/ngeo2721>, 2016.

913 Hersbach, H., Bell, B., Berrisford, S., Hirahara, A., Horányi, J., Muñoz-Sabater, et al.: The ERA5 global reanalysis, *Q. J. R.*  
914 *Meteorol. Soc.*, **146**, 1999-2049, 2020.

915

916 Hewitt, H. T. Hill, R. S. R. Copesey, D. Culverwell, I. D. Harris, C. M. Keen, A. B. McLaren, A. J. et al.: Design and  
917 implementation of the infrastructure of HadGEM3: the next generation Met Office climate modelling system. *Geoscientific*  
918 *Model Development*. **4**(2), 2011.

919 Hirschi, J. J.-M., Barnier, B., Böning, C., Biastoch, A., Blaker, A. T., Coward, A., Danilov, S., Drijfhout, S., Getzlaff, K.,  
920 Griffies, S. M., Hasumi, H., Hewitt, H., Iovino, D., Kawasaki, T., Kiss, A. E., Koldunov, N., Marzocchi, A., Mecking, J. V.,  
921 Moat, B., Molines, J.-M., Myers, P. G., Penduff, T., Roberts, M., Treguier, A.-M., Sein, D. V., Sidorenko, D., Small, J., Spence,  
922 P., Thompson, L., Weijer, W., Xu, X.: The Atlantic meridional overturning circulation in high resolution models, *Journal of*  
923 *Geophysical Research: Oceans*, **125** (4), e2019JC015522. <https://doi.org/10.1029/2019JC015522>, 2020.

924 Huang, B., Thorne, P. W., et. al.: Extended Reconstructed Sea Surface Temperature version 5 (ERSSTv5), Upgrades,  
925 validations, and intercomparisons, *J. Climate*, <https://doi.org/10.1175/JCLI-D-16-0836>, 2017.

926 Hunke, E. C., and Lipscomb, W. H.: Cice: The Los Alamos Sea ice model, documentation and software user's manual, version  
927 4.1 (Tech. Rep.). Los Alamos National Laboratory, 2010.

928 Jackson, R. B. et al.: Increasing anthropogenic methane emissions arise equally from agricultural and fossil fuel sources,  
929 *Environ. Res. Lett.* 15, 071002, 2020.

930 Kanamitsu, M., et al.: NCEP–DOE AMIP-II reanalysis (R-2), *Bull. Amer. Meteor. Soc.*, **83**, 1631–1644,  
931 <https://doi.org/10.1175/BAMS-83-11-1631>, 2002.

932 Keeble, J., Hassler, B., Banerjee, A., Checa-Garcia, R., Chiodo, G., Davis, S., Eyring, V., Griffiths, P. T., Morgenstern, O.,  
933 Nowack, P., Zeng, G., Zhang, J., Bodeker, G., Burrows, S., Cameron-Smith, P., Cugnet, D., Danek, C., Deushi, M., Horowitz,  
934 L. W., Kubin, A., Li, L., Lohmann, G., Michou, M., Mills, M. J., Nabat, P., Olivie, D., Park, S., Seland, Ø., Stoll, J., Wieners,  
935 K.-H., and Wu, T.: Evaluating stratospheric ozone and water vapour changes in CMIP6 models from 1850 to 2100, *Atmos.*  
936 *Chem. Phys.*, 21, 5015–5061, <https://doi.org/10.5194/acp-21-5015-2021>, 2021.

937 Kennedy, J. J., Rayner, N. A., Atkinson, C. P., and Killick, R. E.: An ensemble data set of sea-surface temperature change  
938 from 1850: the Met Office Hadley Centre HadSST.4.0.0.0 data set, *Journal of Geophysical Research: Atmospheres*, 124,  
939 <https://doi.org/10.1029/2018JD029867>, 2019.

940 King B. A.: Objectively mapped Argo profiling float data and RAPID moored microcat data from the North Atlantic Ocean,  
941 2004-2022. NERC EDS British Oceanographic Data Centre NOC. <https://doi.org/10.5285/fe8e524d-7f04-41f3-e053-6c86abc04d51>, 2023.

943

944 Kumar, A., Wu, S., Weise, M. F., Honrath, R., Owen, R. C., Helmig, D., Kramer, L., Val Martin, M. and Li, Q.: Free-  
945 troposphere ozone and carbon monoxide over the North Atlantic for 2001–2011: *Atmospheric Chemistry and Physics*, 13(24),  
946 12537-12547, 2013.

947 Large, W. G., and Yeager, S. G.: The global climatology of an interannually varying air–sea flux data set, *Climate Dynamics*,  
948 33(2), 341– 364. <https://doi.org/10.1007/s00382-008-0441-3>, 2009.

949 Lawler, M. J. et al.: HOCl and Cl<sub>2</sub> observations in marine air, *Atmos. Chem. Phys.*, 11, 7617-7628. 2011.

950 Lee, B. H., Lopez-Hilfiker, F. D., Mohr, C., Kurtén, T., Worsnop, D. R., and Thornton, J. A.: An iodide-adduct high-resolution  
951 time-of-flight chemical-ionization mass spectrometer: Application to atmospheric inorganic and organic compounds,  
952 *Environmental science & technology*, 48(11), 6309-6317, 2018.

953

954 Loades, D. C., Yang, M., Bell, T. G., Vaughan, A. R., Pound, R. J., Metzger, S., Lee, J. D., and Carpenter, L. J.: Ozone  
955 deposition to a coastal sea: comparison of eddy covariance observations with reactive air-sea exchange models, *Atmos. Meas.*  
956 *Tech.*, 13, 6915-6931, [10.5194/amt-13-6915-2020](https://doi.org/10.5194/amt-13-6915-2020), 2020.

957 Lozier, M.S., Li, F., Bacon, S., Bahr, F., Bower, A., Cunningham, S., de Jong, F., de Steur, L., de Young, B., Fischer, J., Gary,  
958 S., Greenan, B., Holliday, N. P., Houk, A., Houpert, L., Inall, M., Johns, B., Johnson, H., Johnson, C., Karstensen, J., Koman,  
959 G., LeBras, I., Lin, X., Mackay, N., Marshall, D., Mercier, H., Oltmanns, M., Pickart, R., Ramsay, A., Rayner, D., Straneo, F.,  
960 Thierry, V., Torres, D., Williams, R., Wilson, C., Yang, J., Yashayaev, I., Zhao, J.: A sea change in our view of overturning  
961 in the Subpolar North Atlantic Program, *Science* 01 Feb 2019:Vol. 363, Issue 6426, pp. 516-521  
962 <https://doi.org/10.1126/science.aau6592>, 2019.

963 Luo, B.: Stratospheric aerosol data for use in CMIP6 models, available at:  
964 [ftp://iacftp.ethz.ch/pub\\_read/luo/CMIP6/Readme\\_Data\\_Description.pdf](ftp://iacftp.ethz.ch/pub_read/luo/CMIP6/Readme_Data_Description.pdf), 2016 .

- 965 Madec et al.: NEMO ocean engine, Note du Po'le de mode' lisation de l'Institut Pierre-Simon Laplace No 27 ISSN No 1288-  
966 1619, 2016.
- 967 Madec, G., and the NEMO System Team: NEMO ocean engine, Scientific Notes of Climate Modelling Center (27) – ISSN  
968 1288-1619, <https://doi.org/10.5281/zenodo.1464816>, 2019.
- 969 Mann, G. W. et al.: “Description and evaluation of GLOMAP-mode: a modal global aerosol microphysics model for the UKCA  
970 composition-climate model”, *Geosci. Mod. Dev.*, 3, 519–551, 2010, <https://doi.org/10.5194/gmd-3-519-2010>, 2010.
- 971 Mann, G. W. et al.: Evolving particle size is the key to improved volcanic forcings, *Past Global Change*, vol. 23, no. 2, 52-53,  
972 <https://doi.org/10.22498/pages.23.2.52>, 2015.
- 973 Matthews, E., Bannan, T. J., Khan, M. A. H., Shallcross, D. E., Stark, H., Browne, E. C., Archibald, A. T., Mehra, A.,  
974 Bauguitte, S. J. B., Reed, C., Thamban, N. M., Wu, H., Barker, P., Lee, J., Carpenter, L. J., Yang, M., Bell, T. G., Allen, G.,  
975 Jayne, J. T., Percival, C. J., McFiggans, G., Gallagher, M., Coe, H: Airborne observations over the North Atlantic Ocean reveal  
976 the importance of gas-phase urea in the atmosphere. *National Academy of Sciences. Proceedings*, 120(25), Article  
977 e2218127120. <https://doi.org/10.1073/pnas.2218127120>, 2023
- 978 Matthews E, Examining novel atmospheric chemistry in the marine environment with an iodide chemical ionisation mass  
979 spectrometer. Ph. D. Thesis. The University of Manchester, 2023.
- 980 McCarthy, G. D., Smeed, D. A., Johns, W. E., Frajka-Williams, E., Moat, B. I. Rayner, D., Baringer, M.O., Meinen, C.S.,  
981 Collins, J., Bryden, H.L.: Measuring the Atlantic Meridional Overturning Circulation at 26°N, *Progress in Oceanography*, 130:  
982 91-111. <https://doi.org/10.1016/j.pocean.2014.10.006>, 2015.
- 983 McFiggans, G. B., et al.: Novel findings in the Reactive Halogens in the Marine Boundary Layer (RHAMBLe) project,  
984 *Geochimica Et Cosmochimica Acta*, 73, A857-A857, 2009.
- 985 Megann, A., Blaker, A., Josey, S., New, A., and Sinha, B.: Mechanisms for late 20th and early 21st Century decadal AMOC  
986 variability, *JGR: Oceans*, 126, e2021JC017865. <https://doi.org/10.1029/2021JC017865>, 2021a.
- 987 Megann, A., Sinha, B., and Blaker, A.: Monthly ocean and sea-ice output from 1/4° NEMO GO6 integration forced by CORE2  
988 data, <https://doi.org/10/gm8vf7>, 2021b .
- 989 Megann, A., Sinha, B. and Blaker, A.: Monthly ocean and sea-ice output from 1/4° NEMO (GO6 integration forced by DFS5.2  
990 data. NERC EDS British Oceanographic Data Centre. <https://doi.org/10/gm8vf5>, 2021c.
- 991 Megann, A., Sinha, B. and Blaker, A.: Monthly ocean and sea-ice output from 1/4° NEMO GO6 integration forced by JRA55  
992 data. NERC EDS British Oceanographic Data Centre. <https://doi.org/10/gm8vf8>, 2021d.
- 993 Megann, A., Sinha, B., Blaker, A., Schroeder, D., Feltham, D.: The North Atlantic Climate System Integrated Study: model  
994 run output. NERC EDS British Oceanographic Data Centre NOC, accessed 27 March 2023,  
995 <http://catalogue.ceda.ac.uk/uuid/770a885a8bc34d51ad71e87ef346d6a8>, 2021e.
- 996 Megann, A., Blaker, A., Coward, A., Guiavarc'h, C., Storkey, D.: Model output from 1/4° global JRA55-forced integration of  
997 GO8p7 global ocean-sea ice model from 1958 to 2021. NERC British Oceanographic Data Centre, 20 October 2022.  
998 doi:10.5285/e02c8424657846468c1ff3a5acd0b1ab, 2022a.
- 999 Megann, A., Blaker, A., Coward, A., Guiavarc'h, C., Storkey, D.: Model output from 1/12° global JRA55-forced integration  
1000 of GO8p7 global ocean-sea ice model from 1958 to 2021, NERC British Oceanographic Data Centre, 20 October 2022.  
1001 doi:10.5285/399b0f762a004657a411a9ea7203493a, 2022b.
- 1002 Middlebrook, A. M., Bahreini, R., Jimenez, J. L., and Canagaratna, M. R.: Evaluation of composition-dependent collection  
1003 efficiencies for the aerodyne aerosol mass spectrometer using field data, *Aerosol Sci. Tech.*, 46, 258–271,  
1004 <https://doi.org/10.1080/02786826.2011.620041>, 2012.

1005 Moat, B. I.; Smeed, D. A.; Frajka-Williams, E.; Desbruyères, D. G.; Beaulieu, C.; Johns, W. E.; Rayner, D.; Sanchez-Franks,  
1006 A.; Baringer, M. O.; Volkov, D.; Jackson, L. C.; Bryden, H. L.: Pending recovery in the strength of the meridional overturning  
1007 circulation at 26° N, *Ocean Science*, 16 (4). 863-874. <https://doi.org/10.5194/os-16-863-2020>, 2020.

1008 Moat, B.I.; King, B.A.; Macintosh, C.R. (2021a): Subpolar North Atlantic ocean heat content (surface to 1000m) using the  
1009 EN4.2.2 temperature data set. NERC EDS British Oceanographic Data Centre NOC, <https://doi.org/10/g6wm>, 2021a

1010 Moat, B. I., King, B. A., Macintosh, C. R.: Subpolar North Atlantic ocean heat content (surface to 1000m) using objectively  
1011 mapped Argo profiling float data, NERC EDS British Oceanographic Data Centre NOC. <https://doi.org/10/g8g2>, 2021b.

1012 Moat, B. I., Frajka-Williams, E., Smeed, D. A., Rayner, D., Johns, W. E., Baringer, M. O., Volkov, D., and Collins, J.: Atlantic  
1013 meridional overturning circulation observed by the RAPID-MOCHA-WBTS (RAPID-Meridional Overturning Circulation and  
1014 Heatflux Array-Western Boundary Time Series) array at 26N from 2004 to 2020 (v2020.2), *British Oceanographic Data Centre*  
1015 - Natural Environment Research Council, UK. <https://doi.org/10.5285/e91b10af-6f0a-7fa7-e053-6c86abc05a09>, 2022.

1016 Monks, P. S., Archibald, A. T., Colette, A., Cooper, O., Coyle, M., Derwent, R., Fowler, D., Granier, C., Law, K. S., Mills, G.  
1017 E., Stevenson, D. S., Tarasova, O., Thouret, V., von Schneidmesser, E., Sommariva, R., Wild, O., and Williams, M. L.:  
1018 Tropospheric ozone and its precursors from the urban to the global scale from air quality to short-lived climate forcer, *Atmos.*  
1019 *Chem. Phys.*, 15, 8889–8973, <https://doi.org/10.5194/acp-15-8889-2015>, 2015.

1020 Morgan, W. T., Allan, J. D., Bower, K. N., Capes, G., Crosier, J., Williams, P. I., and Coe, H.: Vertical distribution of sub-  
1021 micron aerosol chemical composition from North-Western Europe and the North-East Atlantic, *Atmos. Chem. Phys.*, 9, 5389–  
1022 5401, <https://doi.org/10.5194/acp-9-5389-2009>, 2009.

1023 Mulcahy, J. P., Johnson, C., Jones, C. G., Povey, A. C., Scott, C. E., Sellar, A., Turnock, S. T., Woodhouse, M. T., Abraham,  
1024 N. L., Andrews, M. B., Bellouin, N., Browse, J., Carslaw, K. S., Dalvi, M., Folberth, G. A., Glover, M., Grosvenor, D. P.,  
1025 Hardacre, C., Hill, R., Johnson, B., Jones, A., Kipling, Z., Mann, G., Mollard, J., O'Connor, F. M., Palmiéri, J., Reddington,  
1026 C., Rumbold, S. T., Richardson, M., Schutgens, N. A. J., Stier, P., Stringer, M., Tang, Y., Walton, J., Woodward, S., and Yool,  
1027 A.: Description and evaluation of aerosol in UKESM1 and HadGEM3-GC3.1 CMIP6 historical simulations, *Geosci. Model*  
1028 *Dev.*, 13, 6383–6423, <https://doi.org/10.5194/gmd-13-6383-2020>, 2020.

1029 National Centre for Atmospheric Science; Carpenter, L.J.; Hopkins, J.R.; Lewis, A.C.; Neves, L.M.; Moller, S.; Pilling, M.J.;  
1030 Read, K.A.; Young, T.D.; Lee, J.D. (2010): Continuous Cape Verde Atmospheric Observatory Observations. NCAS British  
1031 Atmospheric Data Centre, accessed 31 January, 2024.  
1032 <http://catalogue.ceda.ac.uk/uuid/81693aad69409100b1b9a247b9ae75d5>.

1033 Nisbet, E. G., Manning, M. R., Dlugokencky, E. J., Fisher, R. E., Lowry, D., Michel, S. E., Myhre, C. L., Platt, S. M., Allen,  
1034 G., Bousquet, P. and Brownlow, R.: Very strong atmospheric methane growth in the 4 years 2014–2017: Implications for the  
1035 Paris Agreement, *Global Biogeochemical Cycles*, 33(3), pp.318-342. 2019.

1036 Oltmanns, M., Karstensen, J., Moore, G. W. K., and Josey, S. A.: Rapid cooling and increased storminess triggered by  
1037 freshwater in the North Atlantic, *Geophysical Research Letters*, 47, e2020GL087207, <https://doi.org/10.1029/2020GL087207>,  
1038 2020.

1039 Parrington, M., Palmer, P. I., Henze, D. K., Tarasick, D. W., Hyer, E. J., Owen, R. C., Helmig, D., Clerbaux, C., Bowman, K.  
1040 W., Deeter, M. N., Barratt, E. M., Coheur, P.-F., Hurtmans, D., Jiang, Z., George, M., and Worden, J. R.: The influence of  
1041 boreal biomass burning emissions on the distribution of tropospheric ozone over North America and the North Atlantic during  
1042 2010, *Atmos. Chem. Phys.*, 12, 2077–2098, <https://doi.org/10.5194/acp-12-2077-2012>, 2012.

1043 Phillips, D. P., Hopkins, F. E., Bell, T. G., Liss, P. S., Nightingale, P. D., Reeves, C. E., Wohl, C., and Yang, M.: Air–sea  
1044 exchange of acetone, acetaldehyde, DMS and isoprene at a UK coastal site. *Atmos. Chem. Phys.*, 21, 10111–10132,  
1045 <http://doi.org/10.5194/acp-21-10111-2021>, 2021.

1046 Plymouth Marine Laboratory; Yang, M. (2017): Penlee Point Atmospheric Observatory: Meteorological and chemical  
1047 observations 2014- present. Centre for Environmental Data Analysis, accessed 31 January, 2024.  
1048 <https://catalogue.ceda.ac.uk/uuid/8f1ff8ea77534e08b03983685990a9b0>.

1049 Prather, M. J., Zhu, X., Flynn, C. M., Strode, S. A., Rodriguez, J. M., Steenrod, S. D., Liu, J., Lamarque, J.-F., Fiore, A. M.,  
1050 Horowitz, L. W., Mao, J., Murray, L. T., Shindell, D. T., and Wofsy, S. C.: Global atmospheric chemistry – which air matters,  
1051 *Atmos. Chem. Phys.*, 17, 9081–9102, <https://doi.org/10.5194/acp-17-9081-2017>, 2017.

1052 Priestley, M., Le Breton, M., Bannan, T. J., Leather, K. E., Bacak, A., Reyes-Villegas, E., ... and Percival, C. J.: Observations  
1053 of Isocyanate, Amide, Nitrate, and Nitro Compounds From an Anthropogenic Biomass Burning Event Using a ToF-CIMS,  
1054 *Journal of Geophysical Research: Atmospheres*, 123(14), 7687-7704, 2018.

1055 Ranjithkumar, A., Gordon, H., Williamson, C., Rollins, A., Pringle, K., Kupc, A., Abraham, N. L., Brock, C. and Carslaw, K.:  
1056 Constraints on global aerosol number concentration, SO<sub>2</sub> and condensation sink in UKESM1 using ATom measurements,  
1057 *Atmospheric Chemistry and Physics*, 21(6), pp.4979-5014. 2021.

1058 Read K A. et al.: Extensive halogen-mediated ozone destruction over the tropical Atlantic Ocean, *Nature*, 453, 1232-1235.  
1059 2008.

1060 Reeves, C. E., Penkett, S. A., Bauguitte, S., Law, K. S., Evans, M. J., Bandy, B. J., Monks, P. S., Edwards, G. D., Phillips, G.,  
1061 Barjat, H. and Kent, J.: Potential for photochemical ozone formation in the troposphere over the North Atlantic as derived  
1062 from aircraft observations during ACSOE, *Journal of Geophysical Research: Atmospheres*, 107(D23), pp.ACH-14. 2002.

1063 Reynolds, R. W., Rayner, N. A., Smith, T. M., Stokes, D. C. and Wang, W.: An improved in situ and satellite SST analysis  
1064 for climate, *Journal of climate*, 15(13), pp.1609-1625. 2002.

1065 Ridley, J. K., Blockley, E. W., Keen, A. B., Rae, J. G. L., West, A. E., and Schroeder, D., 2018: The sea ice model component  
1066 of HadGEM3-GC3.1, *Geosci. Model Dev.*, 11, 713–723, <https://doi.org/10.5194/gmd-11-713-2018>. Roberts, Malcolm  
1067 (2017a). *MOHC HadGEM3-GC31-MM model output prepared for CMIP6 HighResMIP highresSST-present*. Version  
1068 20240131. Earth System Grid Federation. <https://doi.org/10.22033/ESGF/CMIP6.6029>.

1069 Roberts, Malcolm (2017b). *MOHC HadGEM3-GC31-HM model output prepared for CMIP6 HighResMIP highresSST-*  
1070 *present*. Version 20240131. Earth System Grid Federation. <https://doi.org/10.22033/ESGF/CMIP6.6024>

1071 Roberts, Malcolm (2018a). *MOHC HadGEM3-GC31-HM model output prepared for CMIP6 HighResMIP hist-1950*. Version  
1072 20240131. Earth System Grid Federation. <https://doi.org/10.22033/ESGF/CMIP6.6040>.

1073 Roberts, Malcolm (2018b). *MOHC HadGEM3-GC31-HH model output prepared for CMIP6 HighResMIP control-1950*.  
1074 Version 20240131. Earth System Grid Federation. <https://doi.org/10.22033/ESGF/CMIP6.5881>.

1075 Roberts, Malcolm (2019a). *MOHC HadGEM3-GC31-MM model output prepared for CMIP6 HighResMIP highresSST-future*.  
1076 Version 20240131. Earth System Grid Federation. <https://doi.org/10.22033/ESGF/CMIP6.6013>.

1077 Roberts, Malcolm (2019b). *MOHC HadGEM3-GC31-HM model output prepared for CMIP6 HighResMIP highresSST-future*.  
1078 Version 20240131. Earth System Grid Federation. <https://doi.org/10.22033/ESGF/CMIP6.6008>.  
1079

1080 Roberts, Malcolm (2019c). *MOHC HadGEM3-GC31-HM model output prepared for CMIP6 HighResMIP highres-future*.  
1081 Version 20240131. Earth System Grid Federation. <https://doi.org/10.22033/ESGF/CMIP6.5984>.

1082 Roberts, M. J., Vidale, P. L., Senior, C., Hewitt, H. T., Bates, C., Berthou, S., et al.: The Benefits of Global High Resolution  
1083 for Climate Simulation: Process Understanding and the Enabling of Stakeholder Decisions at the Regional Scale, *Bulletin of*  
1084 *the American Meteorological Society*, 99(11), 2341–2359. <https://doi.org/10.1175/BAMS-D-15-00320.1>, 2018.

1085 Roberts, M. J., Baker, A., Blockley, E. W., Calvert, D., Coward, A., Hewitt, H. T., et al.: Description of the resolution hierarchy  
1086 of the global coupled HadGEM3-GC3.1 model as used in CMIP6 HighResMIP experiments, *Geoscientific Model*  
1087 *Development*, 12(12), 4999–5028. <https://doi.org/10.5194/gmd-12-4999-2019>, 2019.

1088 Roberts, M. J., Jackson, L. C., Roberts, C. D., Meccia, V., Docquier, D., Koenigk, T., Ortega, P., Moreno-Chamarro, E.,  
1089 Bellucci, A., Coward, A., Drijfhout, S., Exarchou, E., Gutjahr, O., Hewitt, H., Iovino, D., Lohmann, K., Putrasahan, D.,  
1090 Schiemann, R., Seddon, J., Terray, L., Xu, X., Zhang, Q., Chang, P., Yeager, S. G., Castruccio, F. S., Zhang, S., Wu, L.:

- 1091 Sensitivity of the Atlantic meridional overturning circulation to model resolution in CMIP6 HighResMIP simulations and  
1092 implications for future changes. *Journal of Advances in Modeling Earth Systems*, 12 (8), e2019MS002014,  
1093 <https://doi.org/10.1029/2019MS002014>, 2020.
- 1094 Robson, J., Sutton, R. T., Archibald, A., Cooper, F., Christensen, M., Gray, L. J., Holliday, N. P., Macintosh, C., McMillan,  
1095 M., Moat, B., Russo, M., Tilling, R., Carslaw, K., Desbruyères, D., Embury, O., Feltham, D. L., Grosvenor, Daniel P., Josey,  
1096 S., King, B., Lewis, A., McCarthy, G. D., Merchant, C., New, A. L., O'Reilly, C. H., Osprey, S. M., Read, K., Scaife, A.,  
1097 Shepherd, A., Sinha, B., Smeed, D., Smith, D., Ridout, A., Woollings, T., Yang, M.: Recent multivariate changes in the North  
1098 Atlantic climate system, with a focus on 2005-2016, *International Journal of Climatology*, 38 (14), 5050-5076,  
1099 <https://doi.org/10.1002/joc.5815>, 2018.
- 1100 Robson, J., Aksenov, Y., Bracegirdle, T. J., Dimdore-Miles, O., Griffiths, P. T., Grosvenor, D. P., Hodson, D. L. R., Keeble,  
1101 J., Megann, A., Osprey, S., Povey, A. C., Schröder, D., Yang, M., Archibald, A. T., Carslaw, K. S., Gray, L., Jones, C.,  
1102 Kerridge, B., Knappett, D., Kuhlbrodt, T., Russo, M., Sellar, A., Siddans, R., Sinha, B., Sutton, R., Walton, J., Wilcox, L. J.:  
1103 The evaluation of the North Atlantic climate system in UKESM1 historical simulations for CMIP6, *Journal of Advances in*  
1104 *Modeling Earth Systems*, 12 (9), e2020MS002126. <https://doi.org/10.1029/2020MS002126>, 2020.
- 1105 Rollins, A. W., Thornberry, T. D., Ciciora, S. J., McLaughlin, R. J., Watts, L. A., Hanisco, T. F., Baumann, E., Giorgetta, F.  
1106 R., Bui, T. V., Fahey, D. W., and Gao, R.-S.: A laser-induced fluorescence instrument for aircraft measurements of sulfur  
1107 dioxide in the upper troposphere and lower stratosphere, *Atmos. Meas. Tech.*, 9, 4601–4613, [https://doi.org/10.5194/amt-9-](https://doi.org/10.5194/amt-9-4601-2016)  
1108 [4601-2016](https://doi.org/10.5194/amt-9-4601-2016), 2016
- 1109 Russo, M. R., Kerridge, B. J., Abraham, N. L., Keeble, J., Latter, B. G., Siddans, R., Weber, J., Griffiths, P. T., Pyle, J. A., and  
1110 Archibald, A. T.: Seasonal, interannual and decadal variability of tropospheric ozone in the North Atlantic: comparison of  
1111 UM-UKCA and remote sensing observations for 2005–2018, *Atmos. Chem. Phys.*, 23, 6169–6196,  
1112 <https://doi.org/10.5194/acp-23-6169-2023>, 2023.
- 1113 Schiemann, R.; Vidale, P.; Hatcher, R.; Roberts, M. (2019a). *NERC HadGEM3-GC31-HM model output prepared for CMIP6*  
1114 *HighResMIP hist-1950*. Version 20240131. Earth System Grid Federation. <https://doi.org/10.22033/ESGF/CMIP6.6041>.  
1115
- 1116 Schiemann, R.; Vidale, P. L.; Hatcher, R.; Roberts, M. (2019b). *NERC HadGEM3-GC31-HM model output prepared for*  
1117 *CMIP6 HighResMIP highres-future*. Version 20240131. Earth System Grid Federation.  
1118 <https://doi.org/10.22033/ESGF/CMIP6.5985>.
- 1119 Schroeder, D., Feltham, D. L., Tsamados, M., Ridout, A. and Tilling, R.: New insight from CryoSat-2 sea ice thickness for sea  
1120 ice modelling, *The Cryosphere* 13(1), 125-139. ISSN 1994-0424. <https://doi.org/10.5194/tc-13-125-2019>, 2019.
- 1121 Sellar, A. A., Jones, C. G., Mulcahy, J. P., Tang, Y., Yool, A., Wiltshire, A., O'Connor, F. M., Stringer, M., Hill, R., Palmieri,  
1122 J., Woodward, S., de Mora, L., Kuhlbrodt, T., Rumbold, S. T., Kelley, D. I., Ellis, R.; Johnson, C. E., Walton, J., Abraham, N.  
1123 L., Andrews, M. B., Andrews, T., Archibald, A. T., Berthou, S., Burke, E., Blockley, E., Carslaw, K., Dalvi, M., Edwards, J.,  
1124 Folberth, G. A., Gedney, N., Griffiths, P. T., Harper, A. B., Hendry, M. A., Hewitt, A. J., Johnson, B., Jones, A., Jones, C. D.,  
1125 Keeble, J., Liddicoat, S., Mordenstern, O., Parker, R. J., Predoi, V., Robertson, E., Siahann, A., Smith, R. S., Swaminathan,  
1126 R., Woodhouse, M. T., Zeng, G., Zerroukat, M.: UKESM1: description and evaluation of the U.K. Earth System Model,  
1127 *Journal of Advances in Modeling Earth Systems*, 11 (12). 4513-4558. <https://doi.org/10.1029/2019MS001739>, 2019.
- 1128 Sinclair, K., van Dienenhoven, B., Cairns, B., Alexandrov, M., Moore, R., Ziemba, L. D. and Crosbie, E.: Observations of  
1129 aerosol-cloud interactions during the North Atlantic aerosol and marine ecosystem study, *Geophysical Research Letters*, 47(3),  
1130 p.e2019GL085851. 2020.
- 1131 Smyth, T. (2024): ACSIS: Sunphotometer aerosol measurements at Plymouth Marine Laboratory - Version 1. 2001-2023.  
1132 NERC EDS Centre for Environmental Data Analysis, accessed 31 January, 2024,  
1133 <https://catalogue.ceda.ac.uk/uuid/e74491c96ef24df29a9342a3d57b5939>



- 1134 Sommariva, R., Hollis, L. D. J., Sherwen, T., et al.: Seasonal and geographical variability of nitryl chloride and its precursors  
1135 in Northern Europe, *Atmos Sci Lett.*, 19 (8), <https://doi.org/10.1002/asl.844>, 2018.
- 1136 Storkey, D., Blaker, A. T., Mathiot, P., Megann, A., Aksenov, Y., Blockley, E. W., Calvert, D., Graham, T., Hewitt, H. T.,  
1137 Hyder, P., Kuhlbrodt, T., Rae, J. G. L., and Sinha, B.: UK Global Ocean GO6 and GO7: a traceable hierarchy of model  
1138 resolutions, *Geosci. Model Dev.*, 11, 3187–3213, <https://doi.org/10.5194/gmd-11-3187-2018>, 2018.
- 1139 Sutton, R. T., McCarthy, G. D., Robson, J., Sinha, B., Archibald, A. T. and Gray, L. J.: Atlantic multidecadal variability and  
1140 the UK ACSIS program, *Bulletin of the American Meteorological Society*, 99(2), 415–425, 2018.
- 1141 Telford, P. J., Braesicke, P., Morgenstern, O. and Pyle, J. A.: Description and assessment of a nudged version of the new  
1142 dynamics Unified Model, *Atmospheric Chemistry and Physics*, 8(6), 1701–1712, 2008.
- 1143 Thompson, R. L. et al.: Variability in atmospheric methane from fossil fuel and microbial sources over the last three decades,  
1144 *Geophys. Res. Lett.*, 45, 11499–11508, 2018.
- 1145 Tilling, R. L., Ridout, A. and Shepherd, A.: Estimating Arctic sea ice thickness and volume using CryoSat-2 radar altimeter  
1146 data. *Advances in Space Research*, 62(6), pp.1203–1225, 2018.
- 1147 Timmreck, C. et al.: The Interactive Stratospheric Aerosol Model Intercomparison Project (ISA-MIP): motivation &  
1148 experiment design, *Geosci. Mod. Dev.*, 11, 2581–2608, <https://doi.org/10.5194/gmd-11-2581-2018>, 2018.
- 1149 Tsujino, H., et al.: JRA-55 based surface dataset for driving ocean-sea ice models (JRA55-do) *Ocean Modelling*, 130, 79–139,  
1150 <https://doi.org/10.1016/j.ocemod.2018.07.002>, 2018.
- 1151 Turnock, S. T., Butt, E. W., Richardson, T. B., Mann, G. W., Reddington, C. L., Forster, P. M., Haywood, J., Crippa, M.,  
1152 Janssens-Maenhout, G., Johnson, C. E. and Bellouin, N.: The impact of European legislative and technology measures to  
1153 reduce air pollutants on air quality, human health and climate, *Environmental Research Letters*, 11(2), p.024010, 2016.
- 1154 Turnock, S. T., Allen, R. J., Andrews, M., Bauer, S. E., Deushi, M., Emmons, L., Good, P., Horowitz, L., John, J. G., Michou,  
1155 M., Nabat, P., Naik, V., Neubauer, D., O'Connor, F. M., Olivie, D., Oshima, N., Schulz, M., Sellar, A., Shim, S., Takemura,  
1156 T., Tilmes, S., Tsigaridis, K., Wu, T., and Zhang, J.: Historical and future changes in air pollutants from CMIP6 models,  
1157 *Atmos. Chem. Phys.*, 20, 14547–14579, <https://doi.org/10.5194/acp-20-14547-2020>, 2020.
- 1158 Van Pinxteren et al.: Marine organic matter in the remote environment of the Cape Verde islands – an introduction and  
1159 overview to the MarParCloud campaign, *ACP*, *acp-2019-997*, 2020.
- 1160 Walters, D. et al.: The Met Office Unified Model Global Atmosphere 4.0 and JULES Global Land 4.0 configurations, *Geosci.*  
1161 *Model Dev.*, 7, 361–386, <https://doi:10.5194/gmd-7-361-2014>, 2014.
- 1162 White, C., Ussher, S. J., Fitzsimons, M. F., Atkinson, S., Woodward, E. M. S., Yang, M., Bell, T. G.: Inorganic nitrogen and  
1163 phosphorus in Western European aerosol and the significance of dry deposition flux into stratified shelf waters, *Atmospheric*  
1164 *Environment*, 261, 118391, <https://doi.org/10.1016/j.atmosenv.2021.118391>, 2021.
- 1165 Williams, K. D., Copsey, D., Blockley, E. W., Bodas-Salcedo, A., Comer, C. R., Davis, P., et al.: The Met Office Global  
1166 Coupled Model 3.0 and 3.1 (GC3.0 and GC3.1) Configurations, *Journal of Advances in Modeling Earth Systems*, 10, 357–  
1167 380, <https://doi.org/10.1002/2017MS001115>, 2017.
- 1168 Williams, S. D. P., and Berry, D. I.: ACSIS Atlantic Ocean medium resolution SST dataset: Reconstructed 5-day, ½-degree,  
1169 Atlantic Ocean SST (1950–2014). *Geoscience Data Journal*, 7 (2), 135–148, <https://doi.org/10.1002/gdj3.94>, 2020.
- 1170 Wilkinson, M. D., Dumontier, M., Aalbersberg, I. J., Appleton, G., Axton, M., Baak, A., Blomberg, N., Boiten, J. W., da Silva  
1171 Santos, L. B., Bourne, P. E. and Bouwman, J.: The FAIR Guiding Principles for scientific data management and  
1172 stewardship. *Scientific data*, 3(1), 1–9, 2016.
- 1173 Wofsy, S. C., Afshar, S., Allen, H. M., Apel, E., Asher, E. C., Barletta, B., Bent, J., Bian, H., Biggs, B. C., Blake, D. R., Blake,  
1174 N., Bourgeois, I., Brock, C. A., Brune, W. H., Budney, J. W., Bui, T. P., Butler, A., Campuzano-Jost, P., Chang, C. S., Chin,  
1175 M., Commane, R., Correa, G., Crouse, J. D., Cullis, P. D., Daube, B. C., Day, D. A., Dean-Day, J. M., Dibb, J. E., DiGangi,

- 1176 J. P., Diskin, G. S., Dollner, M., Elkins, J. W., Erdesz, F., Fiore, A. M., Flynn, C. M., Froyd, K., Gesler, D. W., Hall, S. R.,  
1177 Hanisco, T. F., Hannun, R. A., Hills, A. J., Hints, E. J., Hoffman, A., Hornbrook, R. S., Huey, L. G., Hughes, S., Jimenez, J.  
1178 L., Johnson, B. J., Katich, J. M., Keeling, R. F., Kim, M. J., Kupc, A., Lait, L. R., Lamarque, J.-F., Liu, J., McKain, K.,  
1179 Mclaughlin, R. J., Meinardi, S., Miller, D. O., Montzka, S. A., Moore, F. L., Morgan, E. J., Murphy, D. M., Murray, L. T.,  
1180 Nault, B. A., Neuman, J. A., Newman, P. A., Nicely, J. M., Pan, X., Paplawsky, W., Peischl, J., Prather, M. J., Price, D. J.,  
1181 Ray, E., Reeves, J. M., Richardson, M., Rollins, A. W., Rosenlof, K. H., Ryerson, T. B., Scheuer, E., Schill, G. P., Schroder,  
1182 J. C., Schwarz, J. P., St. Clair, J. M., Steenrod, S. D., Stephens, B. B., Strode, S. A., Sweeney, C., Tanner, D., Teng, A. P.,  
1183 Thames, A. B., Thompson, C. R., Ullmann, K., Veres, P. R., Vieznor, N., Wagner, N. L., Watt, A., Weber, R., Weinzierl, B.,  
1184 Wennberg, P., Williamson, C. J., Wilson, J. C., Wolfe, G. M., Woods, C. T., and Zeng, L. H.: *ATom: Merged Atmospheric*  
1185 *Chemistry, Trace Gases, and Aerosols*, ORNL DAAC, Oak Ridge, Tennessee, USA, 10.3334/ORNLDAAC/1581, 2018.
- 1186 Yang, M. and Fleming, Z. L.: Estimation of atmospheric total organic carbon (TOC)–paving the path towards carbon budget  
1187 closure, *Atmospheric Chemistry and Physics*, 19(1), 459-471. 2019.
- 1188 Yang, M., Bell, T. G., Hopkins, F. E., and Smyth, T. J.: Attribution of atmospheric sulfur dioxide over the English Channel to  
1189 dimethyl sulfide and changing ship emissions, *Atmos. Chem. Phys.*, 16, 4771–4783, [https://doi.org/10.5194/acp-16-4771-](https://doi.org/10.5194/acp-16-4771-2016)  
1190 2016, 2016a.
- 1191 Yang, M., Bell, T. G., Hopkins, F. E., Kitidis, V., Cazenave, P. W., Nightingale, P. D., Yelland, M. J., Pascal, R. W., Prytherch,  
1192 J., Brooks, I. M., and Smyth, T. J.: Air-sea fluxes of CO<sub>2</sub> and CH<sub>4</sub> from the Penlee Point Atmospheric Observatory on the  
1193 south-west coast of the UK, *Atmospheric Chemistry and Physics*, 16, 5745-5761, <https://doi.org/10.5194/acp-16-5745-2016>,  
1194 2016b.
- 1195 Yang, M., Prytherch, J., Kozlova, E., Yelland, M. J., Parenkat Mony, D., and Bell, T. G.: Comparison of two closed-path  
1196 cavity-based spectrometers for measuring air–water CO<sub>2</sub> and CH<sub>4</sub> fluxes by eddy covariance, *Atmos. Meas. Tech.*, 9, 5509-  
1197 5522, <https://doi.org/10.5194/amt-9-5509-2016>, 2016c.
- 1198 Yang, M., Bell, T. G., Hopkins, F. E., and Smyth, T. J.: Attribution of atmospheric sulfur dioxide over the English Channel to  
1199 dimethyl sulfide and changing ship emissions, *Atmospheric Chemistry and Physics*, 16, 4771-4783,  
1200 <https://doi.org/10.5194/acp-16-4771-2016>, 2016d.
- 1201 Yang, M., Bell, T. G., Brown I. J., Fishwick J. R., Kitidis, V., Nightingale, P. D., Rees, A. P., and Smyth T. J.: Insights from  
1202 year-long measurements of air-water CH<sub>4</sub> and CO<sub>2</sub> exchange in a coastal environment, *Biogeosciences*, 16, 961-978,  
1203 <https://doi.org/10.5194/bg-16-961-2019a>, 2019a.
- 1204 Yang, M., Norris, S. J., Bell, T. G., and Brooks, I. M.: Sea spray fluxes from the southwest coast of the United Kingdom  
1205 dependence on wind speed and wave height. *Atmos. Chem. Phys.*, 19, 15271-15284, [https://doi.org/10.5194/acp-19-15271-](https://doi.org/10.5194/acp-19-15271-2019)  
1206 2019, 2019b.
- 1207 Zawadowicz, M. A., Suski, K., Liu, J., Pekour, M., Fast, J., Mei, F., Sedlacek, A. J., Springston, S., Wang, Y., Zaveri, R. A.,  
1208 Wood, R., Wang, J., and Shilling, J. E.: Aircraft measurements of aerosol and trace gas chemistry in the eastern North Atlantic,  
1209 *Atmos. Chem. Phys.*, 21, 7983–8002, <https://doi.org/10.5194/acp-21-7983-2021>, 2021.